Correlated Wishart ensembles and chaotic time series

Vinayak* and Akhilesh Pandey†
School of Physical Sciences, Jawaharlal Nehru University, New Delhi 110067, India
(Received 21 December 2009; published 4 March 2010)

We study the correlated Wishart ensembles in the context of time series analysis. We are interested in the statistics of eigenlevels, viz. variables associated with independent eigenmodes in the system. The motivation of this work is to study the effect of time series correlations on the Wishart ensembles. In this connection, we derive the level density and the two-point function for the correlated Wishart ensembles by using the binary correlation method. Using our analytic results we analyze spectra of autocovariance matrices derived from single variable stationary time series. We consider the stochastic time series of Gaussian variables with exponentially decaying correlations and time series of chaotic maps, viz. the Arnold map, the Standard map and the stadium billiard map. In both cases, correlated time series are encountered and analyzed under the framework of random matrix theory. It is shown that the eigenlevel statistics for the chaotic maps follow closely those of correlated Wishart ensembles. It is indicated that the presence of collective modes in the spectra of autocovariance matrices is related to the integrability of the system.

DOI: 10.1103/PhysRevE.81.036202 PACS number(s): 05.45.Tp, 02.50.Sk, 89.90.+n, 05.45.Mt

I. INTRODUCTION

In the decades of fifties and sixties, seminal works by Wigner, Dyson, Mehta, Porter, and others [1] led to the foundation of random matrix theory (RMT). Initially, RMT was developed to provide a framework for the statistical study of spectra of complex many-body systems. In due course of time, however, RMT got attention of many physicists as it turned out to be useful in diverse branches of physics.

Random matrices first appeared in mathematical statistics. Wishart [2] introduced ensemble of random matrices of the type $H=AA^{\dagger}$ as a fundamental tool for multivariate analysis where A is $N\times M$ matrix and matrix elements of A are statistically independent Gaussian variables with zero mean and same variance. Matrices H are known as *Wishart matrices* [3] and ensemble of these matrices is known as the Wishart ensemble (WE). For the last two decades, WE has been a subject of many investigations as its applications cover a wide range of complex systems, e.g., quantitative finance [4,5], communication and information theory [6,7], high energy physics [8], quantum entanglement [9], mesoscopic physics [10], biological microarrays [11], Geophysics [12], etc. The Wishart ensemble is also called the Laguerre ensemble [13], because the Laguerre weight function is obtained in the joint probability density (jpd) of the eigenvalues.

Following Dyson's classification [1] of invariant ensembles in RMT one studies Wishart orthogonal ensemble (WOE), Wishart unitary ensemble (WUE), and Wishart symplectic ensemble (WSE). These are analogous to the Gaussian ensembles of random matrices, viz. Gaussian orthogonal ensemble (GOE), Gaussian unitary ensemble (GUE), and Gaussian symplectic ensemble (GSE), which have proved to be useful in the study of quantum chaotic systems [14–16]. These ensembles are invariant respectively under the orthogonal, unitary and symplectic transformations. Dyson index β is often used to refer to O-invariance ($\beta=1$), U-invariance ($\beta=2$), and S-invariance ($\beta=4$). The corresponding matrices are real symmetric, complex Hermitian and real-quaternion self-dual, respectively, for $\beta=1$, 2, and 4. Among the applications of RMT, an important aspect is the universality of spectral fluctuations. Universality claims that, for given β, spectral fluctuations when expressed in terms of unit average spacing for the ensemble of large random matrices are the same, irrespective of the weight function in the jpd of eigenvalues. For instance, spectral fluctuations for the Gaussian and Wishart ensembles are the same [13] for large matrices.

In recent years there has been a revival of interest in the multivariate analysis in time-series studies. RMT (typically $\beta=1$ case) provides a paradigm to understand hidden features of complex correlations. RMT techniques developed in physics [1,14] have proved to be useful in the multivariate analysis also. A prime example of this has been found in the quantitative finance where the empirical correlation matrix, derived from the time series of stock prices of a large set of companies, has been analyzed in the random matrix framework [4,5]. Similar analysis has been used for several other complex systems, e.g., atmospheric variables [17], EEG signals [18], biological microarrays [11], Geophysics [12], etc.

In some of the applications mentioned above and in many other contexts, it becomes necessary to study the cases where entries of the constituting matrix A have correlations along rows or columns or both. Ensembles of such matrices H are known as correlated Wishart ensembles (CWE). The study of CWE differs from that of the WE in the sense that the presence of correlations may lead to nonuniversal spectral statistics. These have been observed in time series of diverse complex systems [4,12,18–20]. For analytic studies we refer to [7,21–25], which have primarily focused on the level density. There has not been a systematic study of the two-point fluctuations nor of the distribution of isolated levels (which we will refer to as the collective modes). The latter has also been of considerable interest in quantitative finance and other data analysis.

*vinayaksps2003@gmail.com
†ap0700@mail.jnu.ac.in

Our main aim in this paper is to obtain results for the level density and for the two-point correlation function by using the binary correlation method, developed earlier by French and his collaborators [14,26,27]. We also derive mean position and fluctuations for isolated levels which are separated from the bulk. The results are valid for large N,M. For the demonstration of our analytic results we analyze stochastic as well as chaotic time series. Our binary correlation result for the two-point function is helpful in fixing the criterion for universal fluctuations in the spectra. We also verify our results for the isolated levels. For the stochastic case we take uncorrelated and correlated Gaussian time series. For the chaotic case, we consider time series from Arnold map, Standard map [28], and stadium billiard map [29]. The analysis confirms our analytic results and gives a test of chaos in the system in spite of the presence of correlations in the time series. We should emphasize that the time series of integrable systems will not follow the RMT predictions. In fact, in the integrable case ensemble of covariance matrices will not be ergodic.

Our paper is organized as follows. In Sec. II, we give definitions and the jpd for CWEs. In Sec. III, we derive the level density by using the binary correlation method. In Sec. IV we derive result for the mean and variance of isolated levels corresponding to the collective modes. In Sec. V, we derive the two-point function. In Sec. VI, we discuss the autcovariance matrices of time series data. In Sec. VII, we use our analytic results for the analysis of stochastic time series with exponentially decaying correlations. In Secs. VIII–X, we analyze time series of chaotic maps, viz. Arnold map, Standard map and stadium billiard map, respectively. In Sec. XI, we briefly discuss the decorrelated ensembles and their spectral statistics. In the final section, we summarize our results.

II. CORRELATED WISHART ENSEMBLES

We consider matrices of type $H=AA^{\dagger}/M$ where $A=\xi^{1/2}B$, ξ is an N-dimensional positive definite symmetric matrix which defines the correlations in each column of A. We consider for completeness all three β values. Matrix elements of B are given by $B_{jk}=B_{jk}^{(0)}$ for $\beta=1$, $B_{jk}=B_{jk}^{(0)}+iB_{jk}^{(1)}$ for $\beta=2$ and $B_{jk}=B_{jk}^{(0)}\mathrm{I}+\Sigma_{\gamma=1}^{3}B_{jk}^{(\gamma)}\tau_{\gamma}$ for $\beta=4$, where I is the two-dimensional identity matrix and the τ_{γ}, for $\gamma=1,2,3$, are the two-dimensional matrix representatives of the quaternion units [1]. For all three β, $B_{jk}^{(\gamma)}$ are real Gaussian variables with zero mean and variance v_{β}^{2} for $\gamma=0,\ldots,\beta-1$. For $\beta=1$, A is real so that $A^{\dagger}=A^{T}$, A^{T} being the transpose of A and for $\beta=2$ and 4, $A^{\dagger}$ represents, respectively, the Hermitian conjugate and dual of A. By construction, H is an N-dimensional hermitian matrix with non-negative eigenvalues. Without loss of generality, we consider $N\leq M$ (otherwise $N-M$ eigenvalues are zero). The ensembles of H are invariant under orthogonal, unitary and symplectic transformations respectively for $\beta=1$, 2, and 4.

The jpd of the matrix elements of B is given by the Gaussian probability measure

$$P(B)dB=\mathrm{C}_{N,\beta}\exp\left[-\mathrm{Tr}\frac{BB^{\dagger}}{2v_{\beta}^{2}}\right]\prod_{j=1}^{N}\prod_{k=1}^{M}\prod_{\gamma=0}^{\beta-1}dB_{jk}^{(\gamma)}, \quad (1)$$

where the prefactor $\mathrm{C}_{N,\beta}$ is the normalization constant. The jpd of the matrix elements of H, has been given by Wishart [2]. For all three β this can be written as [16]

$$P(H)dH\propto(\det\xi)^{-\beta M/2}\det(H)^{[\beta N(\kappa-1)+1-2\beta]/2}\times\exp\left[-\frac{M}{2v_{\beta}^{2}}\mathrm{Tr}(\xi^{-1}H)\right]dH, \quad (2)$$

where $dH=\Pi_{j>k}^{N}\Pi_{\gamma=0}^{\beta-1}dH_{jk}^{(\gamma)}\Pi_{j=1}^{N}dH_{jj}$ is the infinitesimal volume in $N+\beta N(N-1)/2$ dimensional matrix space and $\kappa=M/N$. Variance v_{β}^{2} supplies the scale for the statistics. We fix the scale as $v_{\beta}^{2}=\sigma^{2}\beta^{-1}$. Thus, with bar denoting the ensemble average,

$$\bar{H}=\frac{\overline{AA^{\dagger}}}{M}=\sigma^{2}\xi, \quad (3)$$

which gives the ensemble covariance matrix. We take $\xi_{jj}=1$, for $j=1,\ldots,N$. Then ξ_{jk} represents the correlations coefficient between the elements in jth and kth rows of A.

Matrix H is an *a priori* good model for systems where non-negative definite eigenvalues are encountered. For example, in time series analysis H is the covariance matrix [3–5] and in communication engineering A serves as a model for the channel matrix and H describes the intercarrier interface [30]. Similarly in the study of vibrational spectra of amorphous nanosystems, the Hessian matrix also has a similar structure [31]. We have already mentioned that our interest in CWE is from the perspective of time series analysis where no immediate example is available for $\beta=4$. However, we have included this for the sake of completeness. Nevertheless, this might be useful in quantum transport and other problems.

To obtain the jpd of the eigenvalues from Eq. (2) one needs to integrate over the group of orthogonal, unitary and symplectic matrices respectively for $\beta=1,2$ and 4. Integrations over the group of unitary matrices can be done for CWUE as in [7,23], from where one can derive all the correlation functions in principle. However for $\beta=1$ and 4 it is still an open problem. We use the binary correlation method, which gives exact result for the level density for large matrices and the leading order results for the two-point function. One main advantage of this method is that one can derive results for all three β cases simultaneously [14,26]. Finally we remark that for $\xi=\mathbf{1}$ integrations for all three β cases can be performed, where one finds the Laguerre weight function in the jpd of eigenvalues [1,13].

In the next three sections, we derive our analytic results by using the binary correlation method. Since the study of correlated Wishart ensemble is analogous to the study of transitions to the Gaussian ensembles, we closely follow the method used in [26].

III. LEVEL DENSITY

In the binary correlation method we deal with the resolvents or the Green functions (or the Stieltjes transforms) of

the correlation functions. For instance, to obtain the level density we first derive $G_L(z)$ which is defined as

$$G_L(z) = \left\langle L \frac{1}{z-H} \right\rangle_N. \tag{4}$$

Here L is an arbitrary operator and the angular brackets with subscript N denote the spectral averaging $\langle\Omega\rangle_N = N^{-1}\,\mathrm{Tr}\,\Omega$ for an $N\times N$ matrix Ω. For $L=\mathbf{1}$, Eq. (4) gives the resolvent $G(z)$ for the eigenvalue density $\rho(x)$. Then $\rho(x)$ can be determined uniquely via the relation

$$\rho(x) = \mp \frac{1}{\pi}\Im G(x \pm i\epsilon) = \frac{G(x \mp i\epsilon) - G(x \pm i\epsilon)}{2\pi i}, \tag{5}$$

where ϵ is positive infinitesimal. Defining m_p as the pth moment of $\rho(x)$, i.e., $m_p = \langle H^p\rangle$ and similarly $m_p^L = \langle LH^p\rangle$, for non-negative integer p, we write for large z

$$G_L(z) = \sum_{p=0}^{\infty} z^{-p-1} m_p^L = \sum_{p=0}^{\infty} z^{-p-1}\langle LH^p\rangle_N. \tag{6}$$

It should be noted that the series [Eq. (6)] is not convergent for all z. However, the sum of the convergent series can be extended, except for the branch cut on the real line, to all z by analytic continuation.

For the ensemble averages we obtain from Eq. (1),

$$\overline{B_{jk}^{(\gamma)} B_{lm}^{(\gamma')}} = \frac{\sigma^2}{\beta}\delta_{\gamma\gamma'}\delta_{jl}\delta_{km}. \tag{7}$$

Using Eq. (7), we derive the following exact results valid for arbitrary fixed matrices ϕ and ψ,

$$\frac{1}{M}\langle \overline{B\phi B^\dagger \psi}\rangle_N = \sigma^2\langle\phi\rangle_M\langle\psi\rangle_N, \tag{8}$$

$$\langle \overline{B\phi B\psi}\rangle_N = \frac{(2-\beta)\sigma^2}{\beta}\langle\tilde{\psi}\phi\rangle_N, \tag{9}$$

$$\overline{\langle B\phi\rangle_N\langle\psi B^\dagger\rangle}_N = \frac{\sigma^2}{N}\langle\psi\phi\rangle_N, \tag{10}$$

$$\overline{\langle B\phi\rangle_N\langle B\psi\rangle}_N = \frac{(2-\beta)\sigma^2}{N\beta}\langle\tilde{\psi}\phi\rangle_N. \tag{11}$$

Here [26], $\tilde{\psi}=\psi^T$, $\tilde{\psi}=\psi$ and $\tilde{\psi}=-\tau_2\psi^T\tau_2$, respectively, for $\beta=1$, 2, and 4. Moreover ϕ and ψ are in general rectangular matrices with dimensions suitably adjusted in (8–11). For example, ϕ is $M\times M$ and ψ is $N\times N$ in Eq. (8). These results can also be derived by noting that in each case the average must be given in terms of the quadratic invariants, $\langle\phi\rangle\langle\psi\rangle$, $\langle\tilde{\psi}\phi\rangle$ and $\langle\psi\phi\rangle$. Henceforth, we drop the subscript N for convenience.

It is easy to prove that $\overline{m_0^L} = \langle L\rangle$. Next $\overline{m_1^L} = \langle\overline{LH}\rangle = \sigma^2\langle L\xi\rangle$, which is derived by using Eqs. (3) and (8) with $\phi=\mathbf{1}_{M\times M}$ and $\psi=\mathbf{1}_{N\times N}$. For $p\geq 2$, we consider the following binary associations:

$$\begin{aligned}\overline{m_p^L} &= \frac{1}{M}\langle\overline{L\xi^{1/2}\underbrace{BB^\dagger}\xi^{1/2}H^{p-1}}\rangle \\ &+ \frac{1}{M^2}\sum_{r=0}^{p-2}\langle\overline{L\xi^{1/2}\underbrace{BB^\dagger\xi^{1/2}H^r\xi^{1/2}BB^\dagger}\xi^{1/2}H^{p-r-2}}\rangle \\ &+ \frac{1}{M^2}\sum_{r=0}^{p-2}\langle\overline{L\xi^{1/2}\underbrace{BB^\dagger\xi^{1/2}H^r\xi^{1/2}B}\,B^\dagger\xi^{1/2}H^{p-r-2}}\rangle.\end{aligned} \tag{12}$$

Then by using (8, 9) for these binary associations, we get

$$\begin{aligned}\overline{m_p^L} &= \sigma^2\overline{m_{p-1}^{L\xi}} + \frac{\sigma^2}{\kappa}\sum_{r=0}^{p-2}\overline{m_{p-r-2}^{L\xi}m_{r+1}} + \frac{\sigma^2(2-\beta)(p-1)}{\beta\kappa N}\overline{m_{p-1}^{L\xi}} \\ &= \sigma^2\overline{m_{p-1}^{L\xi}} + \frac{\sigma^2}{\kappa}\sum_{r=0}^{p-2}\overline{m_{p-r-2}^{L\xi}}\,\overline{m_{r+1}}.\end{aligned} \tag{13}$$

Here, the last equality is valid for large N. Equation (13) is valid for $p\geq 1$ where the summation term should take to be 0 at $p=1$. Using these in Eq. (6), we find

$$z\bar{G}_L(z) = \langle L\rangle + \frac{\sigma^2}{\kappa}[\kappa - 1 + z\bar{G}(z)]\bar{G}_{L\xi}(z). \tag{14}$$

This equation can be solved iteratively and we find

$$\bar{G}_L(z) = \left\langle L\left\{z - \frac{\sigma^2}{\kappa}[\kappa - 1 + z\bar{G}(z)]\xi\right\}^{-1}\right\rangle. \tag{15}$$

Finally with $L=\mathbf{1}$, we obtain the resolvent,

$$\bar{G}(z) = \left\langle\left\{z - \frac{\sigma^2}{\kappa}[\kappa - 1 + z\bar{G}(z)]\xi\right\}^{-1}\right\rangle. \tag{16}$$

Equation (16) was first given by Silverstein [25]. This result has been further generalized in [21,22] for an additional M dimensional positive definite matrix η, which represents the correlations in each row of $A(A=\xi^{1/2}B\,\eta^{1/2})$. Since the approximations in both the methods are the same, their result can also be reproduced by our method [32].

Note that Eq. (16) is valid for large N and it depends on the spectrum of ξ. For a nontrivial spectrum of the ξ, it is very difficult to obtain a solution of this equation. Therefore it has to be solved numerically. Equation (16) may be solved iteratively by starting with an initial guess $\bar{G}_{(0)}(x+i\epsilon)$, with $\epsilon\to 0$. Using this as a solution of Eq. (16), we obtain $\bar{G}_{(1)}$ as the first approximation. This is obtained from the sequence

$$\bar{G}_{(n+1)} = F(z,\bar{G}_{(n)}), \quad n=0,1,2,\ldots, \tag{17}$$

where $F(z,\bar{G})$ is given by the right-hand side of the Eq. (16). Next we use $\bar{G}_{(1)}$ in the formula to obtain $\bar{G}_{(2)}$. We continue the process until the solution converges to a desired precision, i.e., $|\bar{G}_{(n+1)} - \bar{G}_{(n)}| \leq \delta$. The final solution, $\bar{G}_{(n)}\to\bar{G}(x)$, can be used as an initial guess for $\bar{G}_{(0)}$ in the neighborhood of x. Following the same process we can numerically evaluate $\bar{G}$ for all x.

In some cases, however, this method fails to converge. For instance, near a sharp cutoff, $\bar{G}$ at x is no longer valid as an initial guess in the neighborhood of x. To tackle such

situations we use the Newton's method. Here, we use the roots of the function $\bar{G}(z)-F[z,\bar{G}(z)]$, for fixed z. Following the standard procedure, we calculate the correction $\delta\bar{G}_{(n)}=\bar{G}_{(n+1)}-\bar{G}_{(n)}$. To the first order in $\bar{G}_{(n)}-F(z,\bar{G}_{(n)})$, we find

$$\delta\bar{G}_{(n)}=-\frac{\bar{G}_{(n)}-F(z,\bar{G}_{(n)})}{\partial(\bar{G}_{(n)}-F(z,\bar{G}_{(n)}))/\partial\bar{G}_{(n)}}. \tag{18}$$

Thus we obtain

$$\bar{G}_{(n+1)}=\bar{G}_{(n)}+\kappa[F(z,\bar{G}_{(n)})-\bar{G}_{(n)}]\times[\kappa-\sigma^2 z\langle\xi[z-\sigma^2\xi(\kappa-1+z\bar{G}_{(n)})/\kappa]^{-2}\rangle]^{-1}. \tag{19}$$

With an initial guess $\bar{G}_{(0)}$ we solve this iteratively. We obtain a rapidly convergent solution for all x.

For the uncorrelated entries of A, $\xi_{jk}=\delta_{jk}$. In this case Eq. (16) is a quadratic equation which yields the level density for the WEs

$$\bar{\rho}(x)=\kappa\frac{\sqrt{(x_+-x)(x-x_-)}}{2\pi x\sigma^2}, \tag{20}$$

valid for $x_-\le x\le x_+$ and 0, otherwise. Here, $x_\pm=\sigma^2(1\pm\kappa^{-1/2})^2$ are the end points of the density. Equation (20) is known as the Marčenko-Pastur law [33], but has also been derived by Dyson [14,33].

IV. COLLECTIVE MODES

Eigenvalues of a covariance matrix are the variances of independent eigenmodes where the eigenmodes are defined by the eigenstates. The eigenmodes, which are dominated by collective behavior, will be called as the "collective modes."

To illustrate this we consider an ensemble correlation matrix for N random variables with zero mean, and unit variance and mutual correlation coefficient c, i.e., $\xi_{jk}=\delta_{jk}+c(1-\delta_{jk})$ for $j,k=1,\ldots,N$. In this case the eigenvalues, ξ_j, are given by

$$\xi_j=\begin{cases}1-c, & j\neq N,\\ Nc+1-c, & j=N.\end{cases} \tag{21}$$

For this spectrum we can write Eq. (16) as

$$\bar{G}(z)=\left\langle Q_N\frac{1}{z-\sigma^2[\kappa-1+z\bar{G}(z)]\xi/\kappa}\right\rangle+\frac{1}{N}\frac{1}{z-\sigma^2[1+c(N-1)][\kappa-1+z\bar{G}(z)]/\kappa}. \tag{22}$$

Here, $Q_k=1-|k\rangle\langle k|$ where $|k\rangle\langle k|$ is the projection operator and $|k\rangle$ is the eigenstate corresponding to the eigenvalue ξ_k. Solving this up to $\mathcal{O}(N^{-1})$ and using the inversion formula, we get

$$\bar{\rho}(x)=\bar{\rho}_0(x)+\frac{1}{N}\delta\left[x-\frac{\sigma^2(Nc+1-c)(Nc\kappa+1-c)}{Nc\kappa}\right], \tag{23}$$

where

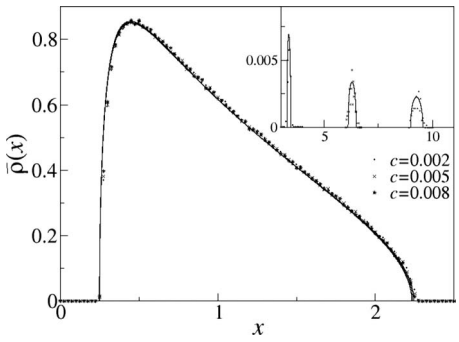

FIG. 1. Level densities obtained from Eq. (22) for $\kappa=4$, $\sigma^2=1$ and for three different values of c. The complete density profile should be seen along with the inset. Solid, dashed and dash-dot lines represent, respectively, the theoretical density for $c=0.002$, 0.005, and 0.008 and circles, crosses, and stars represent the data obtained from simulations in the same order. It should be noted that the differences in the main figure is hardly visible whereas they are more pronounced in the inset where we show distribution of the largest eigenvalue. Also the spreads in the theoretical level densities are the manifest of $\mathcal{O}(N^{-1})$ correction in Eq. (22) whereas in actual calculation it comes from Eq. (30).

$$\bar{\rho}_0(x)=\kappa[2\pi x\sigma^2(1-c)]^{-1}\times\sqrt{4\sigma^4(1-c)^2\kappa^{-1}-[x-\sigma^2(1-c)\kappa^{-1}-\sigma^2(1-c)]^2}. \tag{24}$$

In Eq. (23), the isolated level is obtained from the simple pole in the second term of Eq. (22). In Eq. (24) $\bar{\rho}_0(x)$ corresponds to the density of the uncorrelated case Eq. (20) where the variance σ^2 is replaced by $\sigma^2(1-c)$; it is understood that $\bar{\rho}_0(x)$ is normalized to $1-N^{-1}$. Other $\mathcal{O}(N^{-1})$ terms are associated with the first term of the density and hence are ignored. In the derivation of Eq. (23), we have used

$$\bar{E}=\frac{\sigma^2}{\kappa}[\kappa-1+\bar{E}\bar{G}_0(\bar{E})]\xi_N, \tag{25}$$

where $\bar{E}$ is the ensemble averaged position of the isolated level of H and $\bar{G}_0$ is given by

$$\bar{G}_0(z)=\left\langle Q_N\frac{1}{z-\sigma^2[\kappa-1+z\bar{G}_0(z)]\xi/\kappa}\right\rangle. \tag{26}$$

For the above case it can be simplified. Using Eq. (25) in Eq. (26) we obtain

$$\bar{G}_0(\bar{E})=\frac{\xi_N}{\bar{E}}\left\langle Q_N\frac{1}{\xi_N-\xi}\right\rangle. \tag{27}$$

Now using Eqs. (21) and (27) in Eq. (25)

$$\bar{E}=\sigma^2\frac{(Nc+1-c)(Nc\kappa+1-c)}{Nc\kappa}, \tag{28}$$

giving thereby the isolated level in Eq. (23).

In Fig. 1, we show the level density obtained from the numerical solution of Eq. (22) for different c values. We have also done Monte Carlo simulations of the correspond-

ing ensembles. The Monte Carlo results are shown in the figure by circles, crosses, and stars respectively for $c=0.002$, 0.005, and 0.008. The level density is found to be in agreement with the result [Eq. (23)]. Also, position of the isolated level, $\bar{E}$, is in good agreement with Eq. (27). As shown in the figure, position of the isolated level is very sensitive to c whereas for the level density only the scale varies with c very slowly for small c. In this particular example the collective eigenmode has the largest variance. This type of correlation matrix has been useful in the analysis of financial stock market [4,5,24].

There has been considerable interest on the situations where large number of eigenlevels are separated from the bulk of the spectrum [34,35]. These have been studied in detail but for CWUEs [35]. For such cases, we can generalize our result for the k-th nondegenerate isolated level, ξ_k, of a general matrix ξ as

$$\bar{E} = \frac{\sigma^2 \xi_k}{\kappa}\left(\kappa - 1 + \xi_k \left\langle Q_k \frac{1}{\xi_k - \xi}\right\rangle\right), \tag{29}$$

where ξ_k has moved to position $\bar{E}$. Note that $\bar{E}$ converges to $\sigma^2\xi_k$ as $\kappa \to \infty$. Using the result of the two-point function, given ahead in Eq. (36), variance of E can also be determined to order $\mathcal{O}(\sigma^4 N^{-1})$,

$$\mathrm{var}\{E\} = \frac{2\sigma^2 \xi_k \bar{E}_k}{\kappa \beta N}\left[\frac{1 - \dfrac{\sigma^2 \xi_k^2}{\kappa \bar{E}_k}\left\langle Q_k \xi \dfrac{1}{(\xi_k - \xi)^2}\right\rangle}{1 - \dfrac{\sigma^2 \xi_k}{\kappa \bar{E}_k}\left\langle Q_k \xi \dfrac{1}{\xi_k - \xi}\right\rangle}\right]. \tag{30}$$

We refer to Appendix A for the details of the proof. These results are similar to those [26] for the transitions to Gaussian ensembles: see also [27] for the analogue of Eq. (23).

The isolated level in Eq. (23) is not valid when $\bar{E}$ is in interior of the spectral region $\bar{\rho}_0$. We take $cN = \mathcal{O}(1)$ and use $\bar{E} = x_+ = \sigma^2(\kappa^{-1/2}+1)^2$ to obtain the value of c at which the collective state appears to be outside of $\bar{\rho}_0$. The collective state appears for $c > (N\sqrt{\kappa})^{-1}$. Similar analysis for the general case Eq. (29) is more complicated.

V. TWO-POINT FUNCTION

As for the level density, to obtain the two-point function we deal with the two-point resolvent. The two-point function is defined as

$$S^\rho(x,y) = \overline{\rho(x)\rho(x)} - \bar{\rho}(x)\bar{\rho}(y). \tag{31}$$

It is convenient to deal with the quantity $S^G_{L_1,L_2}(z_1,z_2)$, where L_1 and L_2 are arbitrary operators. $S^G_{L_1,L_2}$ is defined as

$$S^G_{L_1,L_2}(z_1,z_2) = \overline{G_{L_1}(z_1)G_{L_2}(z_2)} - \bar{G}_{L_1}(z_1)\bar{G}_{L_2}(z_2) = \sum_{p,q=0}^{\infty} \frac{\overline{m_p^{L_1} m_q^{L_2}} - \overline{m_p^{L_1}}\,\overline{m_q^{L_2}}}{z_1^{p+1} z_2^{q+1}}. \tag{32}$$

For $L_1 = L_2 = \mathbf{1}$ this simply gives the two-point resolvent $S^G(z_1,z_2)$. Then the two-point function can be calculated by using the inversion formula,

$$S^\rho(x,y) = -\frac{1}{4\pi^2}[S^G(z_1^+,z_2^+) + S^G(z_1^-,z_2^-) - S^G(z_1^-,z_2^+) - S^G(z_1^+,z_2^-)], \tag{33}$$

where we have used $z^\pm = x \pm i\epsilon$.

As in [26], to obtain the double-trace averages we need to consider binary associations of B with B and $B^\dagger$ within the trace and across the traces. Then by using the identities Eqs. (8)–(11), we find

$$\begin{aligned}\overline{m_p^{L_1} m_q^{L_2}} &= \sigma^2 \overline{m_{p-1}^{L_1 \xi} m_q^{L_2}} + \frac{\sigma^2}{\kappa}\sum_{r=0}^{p-2} \overline{m_{p-r-2}^{L_1 \xi} m_{r+1} m_q^{L_2}} \\ &+ \frac{\sigma^2(2-\beta)(p-1)}{\beta \kappa N} \overline{m_{p-1}^{L_1 \xi} m_q^{L_2}} \\ &+ \frac{\sigma^2}{\kappa N^2}\sum_{r=0}^{q-1}\left[\overline{\langle L_1 \xi H^{q-r-1} L_2 H^{p+r}\rangle}\right. \\ &\left. + \frac{2-\beta}{\beta}\overline{\langle L_1 \xi H^{q-r-1} \tilde{L}_2 H^{p+r}\rangle}\right].\end{aligned} \tag{34}$$

In Eq. (34), the first term is valid for $p \geq 1, q \geq 0$, the second and third terms contribute for $p \geq 2, q \geq 0$ and the last two terms contribute for $p,q \geq 1$. Next, we use the expansion $m_\mu^L = \overline{m_\mu^L} + \delta m_\mu^L$, where δm_μ^L is $\mathcal{O}(N^{-1})$ and $\overline{\delta m_\mu^L} = 0$, on both sides of Eq. (34). It is easy to prove that $\overline{\delta m_0 \delta m_q^{L_2}} = \overline{\delta m_p \delta m_0^{L_2}} = 0$ for $p,q \geq 0$. Now the leading order terms are given by

$$\begin{aligned}\overline{\delta m_p^{L_1} \delta m_q^{L_2}} &= \sigma^2 \overline{\delta m_{p-1}^{L_1 \xi} \delta m_q^{L_2}} + \frac{\sigma^2}{\kappa}\sum_{r=0}^{p-2}\left[\overline{\delta m_{p-r-2}^{L_1 \xi} \delta m_q^{L_2}} \bar{m}_{r+1}\right. \\ &\left. + \overline{\delta m_{r+1} \delta m_q^{L_2}}\,\overline{m_{p-r-2}^{L_1 \xi}}\right] \\ &+ \frac{\sigma^2}{\kappa N^2}\sum_{r=0}^{q-1}\left[\overline{\langle L_1 \xi H^{q-r-1} L_2 H^{p+r}\rangle}\right. \\ &\left. + \frac{2-\beta}{\beta}\overline{\langle L_1 \xi H^{q-r-1} \tilde{L}_2 H^{p+r}\rangle}\right].\end{aligned} \tag{35}$$

Note that $\mathcal{O}(N^{-1})$ term in Eq. (35) cancels exactly. Using these in Eq. (32), after some tedious algebra (we refer to Appendix B for details), we obtain finally, a closed form for $S^G(z_1,z_2)$,

$$S^G(z_1,z_2) = \frac{\partial^2}{\partial z_1\, \partial z_2} S^g(z_1,z_2), \tag{36}$$

where

$$S^g(z_1,z_2) = \frac{2}{\beta N^2}\ln\left[1-\frac{\sigma^2}{\kappa}\frac{z_1\bar{G}_\xi(z_1)-z_2\bar{G}_\xi(z_2)}{(z_1-z_2)}\right]$$
$$= \frac{2}{\beta N^2}\ln\left[\frac{\kappa(\kappa-1)-\dfrac{z_1z_2\kappa[\bar{G}_1-\bar{G}_2]}{z_1-z_2}}{(\kappa-1+z_1\bar{G}_1)(\kappa-1+z_2\bar{G}_2)}\right]. \quad (37)$$

Here, $\bar{G}_\xi$ is given by Eq. (15) with $L=\xi$. See [26] for the analogous result for transitions to the Gaussian ensembles. The result for the uncorrelated Wishart ensembles has been recently given in [36]. The last equality is derived from the first one by using Eq. (16), where subscripts {1,2} denote, respectively, z_1 and z_2 dependence.

For the two-point resolvent $S^g(z_1,z_2)$, we consider the two-point function $S^F(x_1,x_2)$ which corresponds to the distribution function $F(x)=\int_{-\infty}^{x}dx'\rho(x')$. S^F is related to S^ρ via

$$S^\rho(x,y) = \frac{\partial^2}{\partial x\,\partial y}S^F(x,y). \quad (38)$$

For inversion it is easier to start with S^F. The inversion formula relating S^F to S^g is the same as the formula (33) relating S^ρ to S^G. We consider the density $\bar{\rho}$ to be a smooth function of x, so that it can be differentiated. Writing

$$G(x\pm i\epsilon) = \mathbf{P}(x) \mp i\pi\rho(x), \quad (39)$$

where $\mathbf{P}(x)=\Re[G(x\pm i\epsilon)]$ is the principal value integral of the density, we find

$$S^F(x,y) = -\frac{1}{2\beta\pi^2N^2}\ln\left[\frac{\left[\left(1-\frac{1}{\kappa}-\frac{x^2}{\kappa}\frac{\partial\bar{\mathbf{P}}}{\partial x}\right)^2+\frac{\pi^2x^4}{\kappa^2}\left(\frac{\partial\bar{\rho}}{\partial x}\right)^2\right]}{\left(1-\frac{1}{\kappa}-\frac{x^2}{\kappa}\frac{\partial\bar{\mathbf{P}}}{\partial x}\right)^2+\frac{4\pi^2x^4\bar{\rho}^2}{\kappa^2(x_1-x_2)^2}}\right], \quad (40)$$

where $x=(x_1+x_2)/2$ describes the mean position. Finally, for the unfolded spectra, we write $N\bar{\rho}|x_1-x_2|=r$ and obtain

$$S^F(x,y) = -\frac{1}{2\beta\pi^2N^2}\times\ln\left\{\frac{r^2\left[\left(\frac{\kappa-1}{x^2}-\frac{\partial\bar{\mathbf{P}}}{\partial x}\right)^2+\pi^2\left(\frac{\partial\bar{\rho}}{\partial x}\right)^2\right]}{r^2\left(\frac{\kappa-1}{x^2}-\frac{\partial\bar{\mathbf{P}}}{\partial x}\right)^2+4\pi^2\bar{\rho}^4N^2}\right\}. \quad (41)$$

This result is valid for $r\gtrsim 1$ and is analogous to the result given for transitions to the Gaussian ensembles in [26].

The correspondence of universal spectral fluctuations with the two-point function (41) may be understood from the following criterion. Consider

$$2\pi\bar{\rho}^2N \gg \left|\left(\frac{1-\kappa}{x^2}-\frac{\partial\bar{\mathbf{P}}}{\partial x}\right)r\right|. \quad (42)$$

Since the unfolded two-point function follows as the double differential of $(-N^2S^F)$ with respect to r, we obtain from Eqs. (41) and (42),

$$\frac{S^\rho(x,y)}{\bar{\rho}(x)\bar{\rho}(y)} = -\frac{1}{\beta\pi^2r^2}. \quad (43)$$

This is the same result as given for the Gaussian [26] and Wishart ensembles [13], implying thereby universal fluctuations in the cases where Eq. (42) is satisfied. On the other hand, spectral fluctuations deviate from the universality when the inequality Eq. (42) is not valid. This criterion may be useful in the spectral analysis of correlated Wishart matrices encountered in various complex systems. In the rest of the paper, we demonstrate the validity of the above results for several stochastic and chaotic time series.

VI. WISHART ENSEMBLES AND AUTOCOVARIANCE MATRICES

To derive the autocovariance matrix of the time series of a single variable one can consider M time series, derived from M randomly chosen initial conditions, each of length N with mean 0. Next, we arrange the time series side by side columnwise and identify the matrix as A. Then the autocovariance matrix can be derived from A by calculating $AA^\dagger/M$. However, we consider the examples where for a given initial condition the whole matrix A is derived from the time series of length NM of the same initial condition. We construct the matrix A by consecutive sections of the time series of length N and writing each section columnwise. As shown in the subsequent sections, this fits our random matrix model provided the autocorrelation function dies rapidly on a time scale $\lesssim N$.

Let X_μ with $\mu=1,\ldots,NM$ be the time series being analyzed where the mean and variance of X_μ are 0 and σ^2, respectively. Matrix elements of A are given by $A_{jk}=X_{(k-1)N+j}$ where $j=1,\ldots,N$, $k=1,\ldots,M$. Then the ensemble average of H is simply $\sigma^2\xi$ where ξ is the ensemble correlation matrix. Here, the ensemble is defined with respect to initial conditions. Note that for a single variable time series $\xi_{jk}=C(|j-k|)$ where $C(\zeta)$ is the autocorrelation function of the time series (i.e., the correlation coefficient between X_μ and $X_{\mu+\zeta}$). Let $C(\zeta)\approx 0$ for $\zeta\gg\zeta_\ell$ where ζ_ℓ is the correlation length and is $\lesssim N$. Then we have

$$\overline{A_{j\ell}A_{km}} = \overline{X_{j+(\ell-1)N}X_{k+(m-1)N}} = \sigma^2C(|(j-k)+N(\ell-m)|). \quad (44)$$

For $\ell=m$, this gives $\sigma^2\xi_{jk}$. For $\ell-m=\mathcal{O}(1)$ there may be non-zero contributions when $\zeta_\ell\sim\mathcal{O}(N)$ but contribution of such terms to moments is $\mathcal{O}(N^{-1})$. Thus, one can consider X_μ as M independent realizations of N variables. As mentioned above, some authors also consider a symmetric matrix η of dimension M to account for the correlations in each row of A [7,21,22]. In our case $\eta=\mathbf{1}$, since the autocorrelation dies rapidly. Moreover, in the case of stronger correlations, one

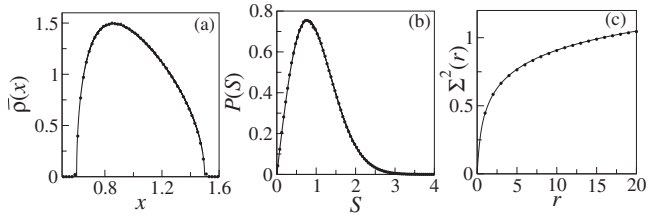

FIG. 2. Numerical results for $c=0$. Solid lines represent RMT and dots represent simulation. Figure (a) gives the level density Eq. (20) and figures (b) and (c) give respectively the spacing distribution Eq. (45) and the number variance Eq. (46). Solid lines represent RMT and dots represent simulations.

needs to deal with more complicated models which take account of the correlations across rows and columns.

We consider 1000 independent times series X_μ of length NM, where $N=1000$ and $M=20\,000$, in most of the examples below. The exceptional cases are the Standard map and the stadium billiard map ($L=0.5$), where 500 independent time series are used. In all the examples below we use the theoretical density to unfold the eigenlevel spectra and compute numerically the fluctuation measures, viz., $P(S)$ and $\Sigma^2(r)$ given for the GOE (and hence for WOE), respectively, by

$$P(S) = \frac{\pi}{2} S \exp(-\pi S^2/4), \tag{45}$$

$$\Sigma^2(r) = \frac{2}{\pi^2}\left[\ln(2\pi r) + \gamma + 1 - \frac{\pi^2}{8}\right]. \tag{46}$$

Here in Eq. (45), $P(S)$ is the spacing distribution, viz. density of the nearest neighbor spacings with unit average. In Eq. (46), $\Sigma^2(r)$ is the number variance, viz. variance of the number of levels in intervals r containing on the average r levels. $P(S)$ gives an indication of level repulsion in the system while $\Sigma^2(r)$ measures the spectral rigidity of the spectrum.

VII. STOCHASTIC TIME SERIES WITH EXPONENTIALLY DECAYING CORRELATIONS

We consider the time series X_μ of stochastic variables where the correlation between X_n and $X_{n+\zeta}$ decays exponentially,

$$C(\zeta) = \overline{X_n X_{n+\zeta}} = c^\zeta, \tag{47}$$

where $1 \geq |c| \geq 0$ and $n \geq 1$. For small values of $|c|$, ξ has approximately banded profile near the diagonal. For $c=1$, X_μ

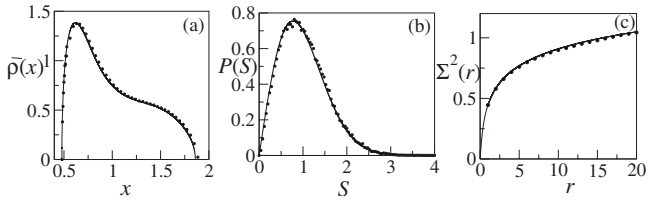

FIG. 3. Numerical results for $c=0.2$; shown on the same pattern of Fig. 2.

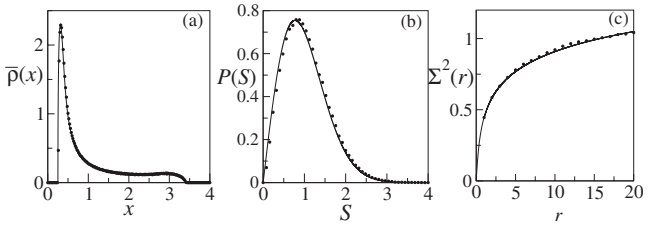

FIG. 4. Numerical results for $c=0.5$; shown on the same pattern of Fig. 2.

is the time series of perfectly correlated variable where no statistics is expected. For $c=0$, X_μ is the time series of independent variables, i.e., $\xi_{jk}=\delta_{jk}$.

As shown in Fig. 2(a), for $c=0$, the numerical density of eigenlevels is that of the WOE [Eq. (20)] and follows closely the Marčenko-Pastur density. The fluctuation measures $P(S)$ and $\Sigma^2(r)$, are shown respectively in Figs. 2(b) and 2(c) and are in agreement with the GOE predictions.

Now, we consider small correlations by choosing $c=0.2$. We obtain the ξ spectrum in the range $0.667 \leq \xi_j \leq 1.499$ where almost 56% levels are having values <1. Effects of this can be seen in Fig. 3(a) where large number of levels are found to be <1 and the level density attains larger span, $0.478 \leq x \leq 1.859$. The theoretical density is obtained from the numerical solution of Eq. (16) by using the spectrum of ξ. This matches well with the density obtained from the simulation. The fluctuation measures are also found to be consistent with universal predictions as shown in Figs. 3(b) and 3(c), respectively, for $P(S)$ and $\Sigma^2(r)$.

Next we consider moderate correlations by choosing $c=0.5$. Here, the spectrum of ξ is obtained in the range $0.3334 \leq \xi_j \leq 3$ where 66.7% levels are having value <1. In comparison to the $c=0.2$ case we obtain here larger span in the density, $0.251 \leq x \leq 3.3738$, and larger number of eigenlevels near the lower cut-off: compare Fig. 4(a) with Fig. 3(a). Spacing distribution and number variance are again in good agreement with universal predictions, as shown, respectively, in Figs. 4(b) and 4(c).

Finally, we consider strong correlations where $c=0.9$. Here, off-diagonal band of the correlation matrix is much

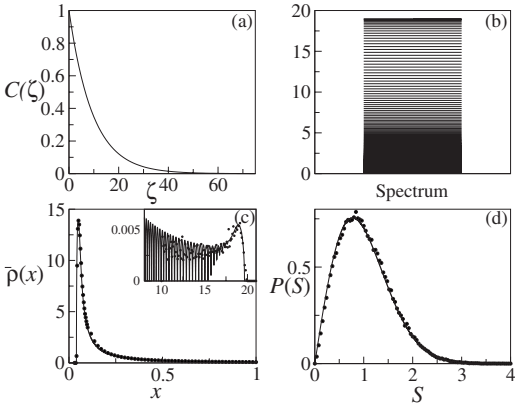

FIG. 5. Numerical results for $c=0.9$. In figure (a) we have shown $C(\zeta)$ vs ζ. Figure (b) represents the ξ spectrum. Figure (c) shows the level density $\bar{\rho}(x)$ and figure (d) is for the spacing distribution.

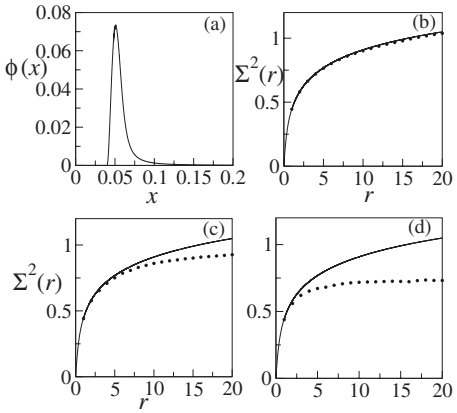

FIG. 6. Numerical results for $c=0.9$. Figure (a) is $\Phi(x)$ vs x and figure (b), (c) and (d) are the number variance graphs, respectively, for $0.045 \le x \le 0.15, 0.15 \le x \le 0.3$ and $0.3 \le x \le 1.0$.

larger than the previous two cases, yet much smaller than the dimension of matrix. The off-diagonal matrix elements are found to be non-zero up to $|j-k| \approx 50$ as suggested by $C(\zeta)$ shown in Fig. 5(a). The ξ spectrum, shown in Fig. 5(b), ranges from 0.0526 to 18.9837 where 85.6% levels are having values <1. The level density follows the same trend as observed in the previous cases. Here again, we obtain majority of the eigenlevels near the lower cut-off. The level density is obtained in the range $0.04 \le x \le 19.492$. We have shown the density for $0.039 \le x \le 1$ in Fig. 5(c) and tail of the density in the inset. Again the density as well as the spacing distribution are found to be in agreement with the universal results as shown in Fig. 5(c) and 5(d), respectively. In Fig. 6(a), we plot the comparison function

$$\Phi(x) = \frac{2\pi\bar{\rho}^2}{|(1-\kappa)x^{-2} - \partial\overline{\mathbf{P}}/\partial x|}. \tag{48}$$

In Sec. V, we have given the analysis of the two-point function where the universal behavior of the spectrum is obtained

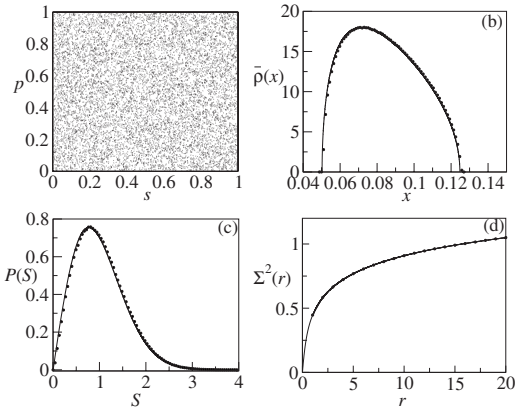

FIG. 7. Numerical results for the s variable of the Arnold map. Figure (a) shows s vs p phase plot of the Arnold map obtained from 10^4 iterations. In figures (b), (c), and (d) we have shown respectively the level density, spacing distribution and number variance for the s variable. For figures (b), (c), and (d) solid lines represents RMT and dots represent simulations. The similar results are obtained for the p variable.

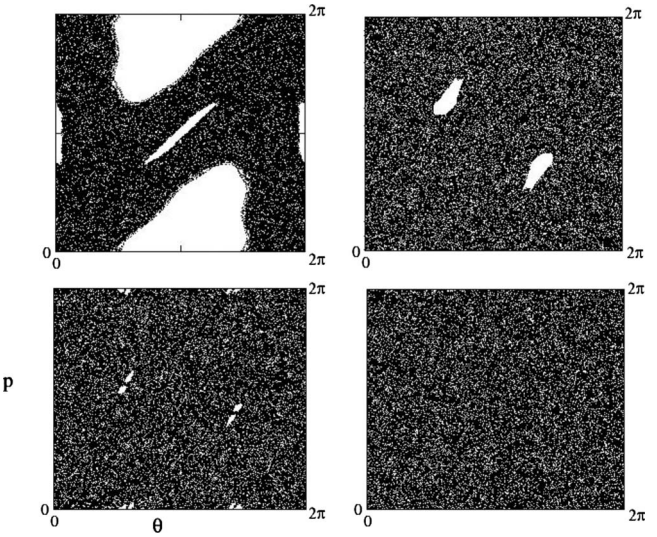

FIG. 8. θ vs p phase plots in the chaotic region of the Standard map with kicking strength $K=2$, and 5 in the upper boxes, respectively from left to right. Phase plots for $K=9.26$ and 10, are shown in the lower boxes, respectively, from left to right. As shown here, there are small islands for $K=9.26$, which disappear for $K=10$.

when $\Phi N \gg r$, i.e., $\Phi \gg N^{-1}$ for $r \sim \mathcal{O}(1)$. As predicted by the comparison plot, GOE result for $\Sigma^2(r)$ is found only for the range $0.04 < x < 0.15$ containing roughly around 600 eigenlevels from each spectrum: see Fig. 5(b). Departure from the universality is found for $0.15 < x < 1.0$, which becomes prominent for larger value of x. These are shown in Figs. 5(c) and 5(d), respectively, for the ranges $0.15 < x < 0.3$ and $0.3 < x < 1.0$. In the range $0.15 < x < 1.0$ there are roughly around 200 eigenlevels from each spectrum. The density becomes multimodal in the tail $(x > 1)$. As expected, these modes merge with each other as we increase N.

VIII. ARNOLD MAP

For the chaotic systems we first consider the Arnold map. The map is given by

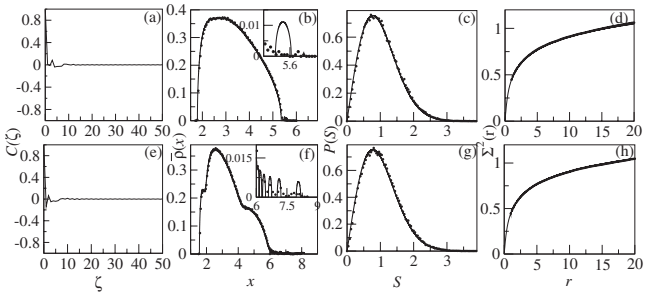

FIG. 9. $C(\zeta)$, $\bar{\rho}(x)$, $P(S)$, and $\Sigma^2(r)$ from left to right for the θ and p variables in the chaotic region (c.f. Fig. 8) of the Standard map for $K=5$. Upper boxes are for the θ variable and lower boxes are for the p variable. One collective mode is observed in the level density for the θ variable as shown in the inset of Fig. 9(b). Five collective modes are observed for the p variable as shown in the inset of Fig. 9(f).

TABLE I. Table of $\bar{E}_j$ corresponding to the collective modes shown in the inset of Fig. 9(f), for the p variable of the Standard map with kicking strength $K=5$.

j (Index)	$\sigma^2\xi_j$	$\bar{E}_j$ (Theory)	$\bar{E}_j$ (Simulation)
996	5.6879	6.2004	6.1992
997	5.9100	6.3783	6.3668
998	6.2556	6.6739	6.6501
999	6.7407	7.1149	7.0948
1000	7.7454	8.0646	8.0920

$$s_{n+1} = s_n + p_n, \quad (\mathrm{mod}\ 1),$$

$$p_{n+1} = s_n + 2p_n, \quad (\mathrm{mod}\ 1). \tag{49}$$

In Fig. 7(a) we have shown the phase plot of Arnold map for 10^4 iterations. For the length of time series we have considered, the phase space has been explored almost everywhere. We have done analysis for the time series of s and p both. For both variables the autocorrelation function, $C(\zeta)$, falls off very rapidly ($C(\zeta) \approx 10^{-5}$ even for $\zeta=1$). In Figs. 7(b)–7(d) we show the results for the s variable (the p variable gives similar result). As shown in Fig. 7(b), the level density is well described by the density Eq. (20) given for uncorrelated case. The fluctuation measures are also found to be in good agreement with Eqs. (45) and (46).

IX. STANDARD MAP

We consider the chaotic region of the Standard map (or Kicked rotor). The map is given by

$$p_{n+1} = p_n + K \sin\theta_n, \quad (\mathrm{mod}\ 2\pi),$$

$$\theta_{n+1} = \theta_n + p_{n+1}, \quad (\mathrm{mod}\ 2\pi), \tag{50}$$

where θ_n is the angle of rotor, p_n is the conjugate momentum and K is the kicking strength. We have considered both variables with kicking strength $K=2$, 5, 9.26, and 10. Phase plots of the chaotic regions of the standard map are shown in Fig. 8. The chaotic region grows with K and covers nearly the entire phase space for $K=10$.

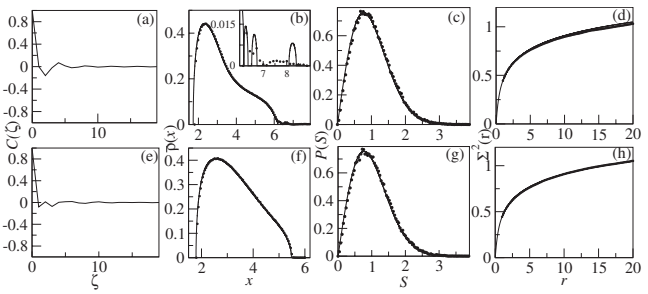

FIG. 10. Numerical results obtained from the analysis of the time series of both the variables of the Standard map for $K=9.26$. These are shown on the same pattern of Fig. 9.

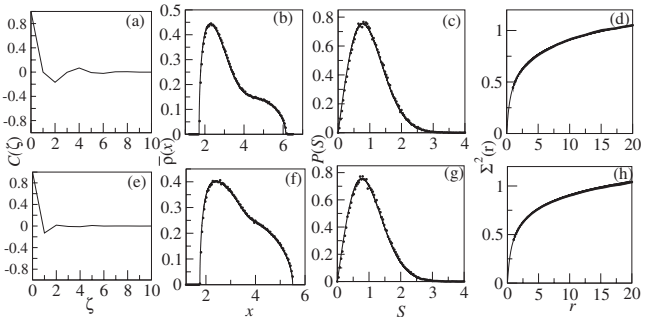

FIG. 11. Numerical results obtained from the analysis of the time series of both the variables of the Standard map for $K=10$. Unlike the $K=5$ and 9.26, no collective behavior is observed in the spectra.

As mentioned before, we have considered 500 independent time series. For $K=10$ and 100, σ^2 is found to be close to the predicted value $(2\pi)^2/12$, for both the variables. For $K=2$, 5, and 9.26, the phase space is not fully explored in which case the initial conditions has to be chosen from the chaotic regions of the phase space and σ^2 has to be determined numerically.

In Figs. 9–12, we show the numerical results, respectively, for $K=5$, 9.26, 10, and 100, respectively. For both variables, $C(\zeta)$ is oscillatory but decays rapidly. The theoretical level density gives a good account of the observed level density. In the level densities we observe situations where some eigenvalues are found to be away from the bulk. For the θ variable, one collective mode has been obtained for $K=5$: see Fig. 9(b). For the p variable, we find five collective modes: see Fig. 9(f). For $K=9.26$, three collective modes have been obtained for the θ variable, while there is no collective for the p variable: see Figs. 10(b) and 10(f) for the respective variables. In Fig. 11 we show results for $K=10$. In this case no collective mode is obtained for both the variables. The spacing distribution and the number variance are shown along with $C(\zeta)$ and $\bar{\rho}(x)$ for the respective variables and K. In all the three cases, the level density as well as the fluctuation measures are found to be in good agreement with the GOE. For $K=100$, the autocorrelation functions die rapidly for both variables, as in the Arnold map. Therefore the statistics follow those of the uncorrelated WE: see Fig. 12.

For $K=5$, we have given the ensemble averaged position of the jth level, $\bar{E}_j$ for $j=996,\ldots,1000$, along with the cor-

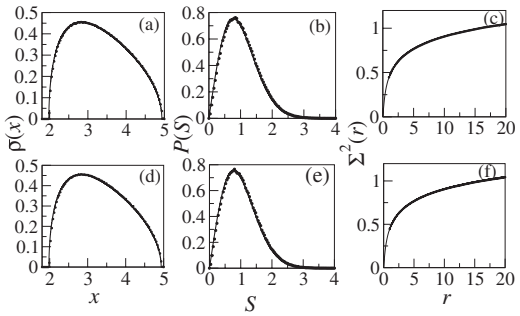

FIG. 12. $\bar{\rho}(x)$, $P(S)$, and $\Sigma^2(r)$ from left to right for the θ and p variables of the Standard map where $K=100$. Upper boxes are for the θ variable and lower boxes are for the p variable.

TABLE II. Table for the $\bar{E}_j$ corresponding to the collective modes shown in the inset of Fig. 10(b), for the θ variable of the Standard map with kicking strength $K=9.26$. However the agreement between theory and simulation is misleading because each of the corresponding ξ_j is nearly doubly degenerate, in which case (29) should be modified to take account of the degeneracies.

j (Index)	$\sigma^2\xi_j$	$\bar{E}_j$ (Theory)	$\bar{E}_j$ (Simulation)
998	5.7370	6.2687	6.2575
999	6.1868	6.6202	6.6040
1000	7.9478	8.2453	7.9667

responding ξ_js in Table I. We have calculated $\bar{E}_j$ by using the ξ_js in Eq. (29) and from the spectra. For the s variable, using the spectra, we find $\bar{E}_{1000}=5.6467$. This is close to the value, 5.5588, obtained from Eq. (29). As shown in Table I for the p variable, numerical values of the $\bar{E}_j$s, are close to the theory Eq. (29). The same is true for the θ variable for $K=9.26$, as given in the Table II.

For $K=2$, the phase plot is not fully explored. For the θ variable the ξ spectrum is obtained in the range $0.3266 \le \xi_j \le 3.8458$. This is shown in Fig. 13(b). The level density is obtained in the range $1.0202 \le x \le 18.50$, and is shown in Fig. 13(c). Following the two-point comparison plot, shown in Fig. 15(a), we have analyzed the spectra for the three rigions, viz. (i) $1.0420 \le x \le 1.71$, (ii) $1.90 \le x \le 4.32$ and (iii) $4.32 \le x \le 11.10$. Region (i) contains roughly around 255 levels, (ii) contains roughly around 435 levels and (iii) contains roughly around 242 levels from each spectrum. As shown in Figs. 16(a)–16(c), respectively, for (i), (ii) and (iii), spacing distribution is consistent with the GOE. On the other hand the number variance deviates from the GOE and tends towards the Poisson statistics, for all the three spectral regions. The number variances are shown in Figs. 17(a)–17(c), respectively, for (i), (ii), (iii). In these figures we have also considered results of the matrices of smaller size ($N=200$). These figures show the finite-N effect in the analysis. The deviations are because of the small inconsistency (not visible in the figures) of the data with theory for the level density, leading to improper unfolding. This can be removed by considering even larger dimensional matrices.

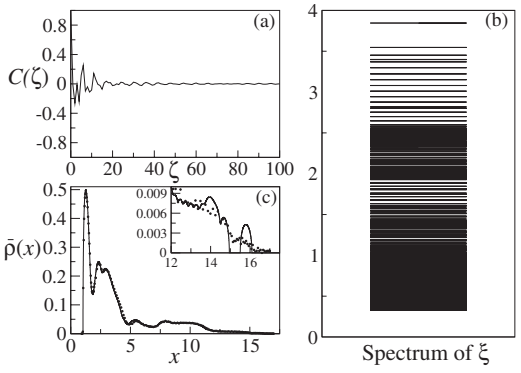

FIG. 13. Numerical results for the θ variable for $K=2$. Figure (a) is for $C(\zeta)$ vs ζ. In figure (b) we show the ξ spectrum. The level density is shown in figure (c) where tail of the density is shown in the inset of figure (c).

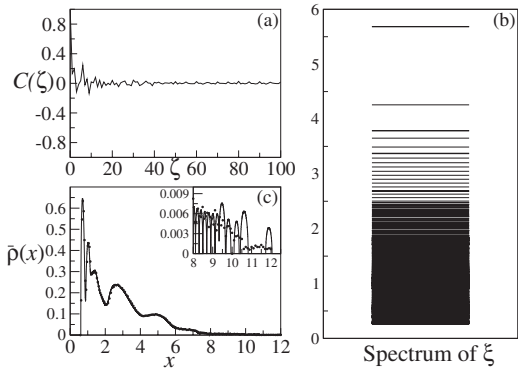

FIG. 14. Numerical results for the p variable for $K=2$. Figure (a) is for $C(\zeta)$ vs ζ. In figure (b) we show the ξ spectrum. The level density is shown in figure (c). The tail of the density has several collective modes as shown in the inset of figure (c).

For the p variable the ξ spectrum is found in the range $0.2661 \le \xi_j \le 5.6862$ whereas the density is found in the range $0.6056 \le x \le 19.669$. The ξ spectrum and the level density are shown respectively in Figs. 14(b) and 14(c). Following the two-point comparison plot, given in Fig. 15(b), here also we have analyzed the spectra for the three regions, viz. (i) $0.6147 \le x \le 2.14$, (ii) $2.14 \le x \le 4.0$, and (iii) $4.0 \le x \le 5.71$ where (i) contains roughly around 446 levels, (ii) contains roughly around 335 levels, and (iii) contains roughly around 158 levels from each spectrum. We have obtained results for the spacing distribution and for the number variance as for the θ variable. The spacing distribution is consistent with the GOE for the three regions as shown respectively in Figs. 16(d)–16(f) for (i), (ii), and (iii). The number variances are also shown, in Figs. 17(d)–17(f), in the same order; the number variance shows the same departures as in the case of the θ variable.

X. STADIUM BILLIARD MAP

Our third example is the stadium billiard map where we deal again with time series of the s and p variables separately. The stadium billiard map is given in Appendix C. The shape of the stadium billiard is shown in Fig. 18. s vs p

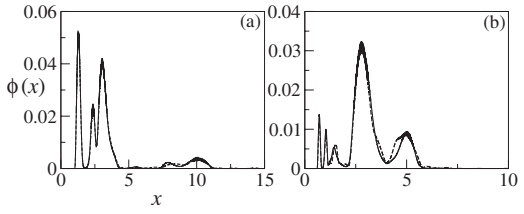

FIG. 15. $\Phi(x)$ vs x for the θ and p variable respectively in figure (a) and (b) for $K=2$. Solid line corresponds to $N=1000$ where as dashed line corresponds to lower dimensional matrices where $N=200$. Note that $\Phi(x)$ is independent of N and GOE is valid when $\Phi(x) \gg N^{-1}$.

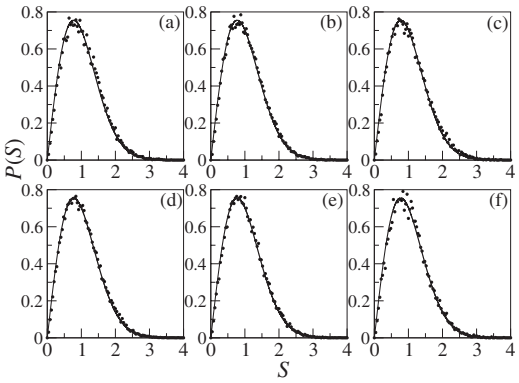

FIG. 16. Spacing distribution for $K=2$ for θ and p variable of the Standard map. Figures (a), (b), and (c) are for the θ variable respectively for the ranges (i), (ii), and (iii) given in text. Figures (d), (e), and (f) are respectively for ranges (i), (ii), and (iii) of the p variable. Solid lines represent GOE, and dots represent simulations.

phase plots for different values of the length L are shown in Fig. 19 where we have fixed the radius $R=1$. As shown in the figure, the phase space is fully covered by the trajectories for 10^5 iterations when $L=0.1, 0.5, 1.0$. However, even for 10^5 iterations, for $L=0.01$ the phase plot is not fully explored. For such small values of L cantori (remnants of tori) are observed. When the system becomes ergodic, the scale is given by $\sigma^2=(\text{perimeter})^2/12$ and $\sigma^2=1/3$, respectively, for the s and p variables. The autocorrelation function, for both variables, is sensitive to L/R. For $L/R\leq 1$, $C(\zeta)$ is oscillatory for the s variable and is stretched exponential for the p variable. On the other hand when $L/R>1$, it becomes oscillatory for both. In the analysis we have fixed $R=1$ and considered $L=1.0$ and 0.5.

We begin with time series of the s variable for $L=1$. The autocorrelation function of the s variable is oscillatory and decays rapidly ($|C(\zeta)|\approx 10^{-2}$ for $\zeta\geq 20$ and $|C(\zeta)|\approx 10^{-3}$ for $\zeta\geq 70$). This is shown in Fig. 20(a). Spectrum of ξ is shown in Fig. 20(b) where $0.567\,054\leq\xi_j\leq 4.685\,76$. Level density is obtained in the range $2.4850\leq x\leq 26.7369$ and is shown in Fig. 20(c). Majority of levels have values ≤ 12.88 (including the level spreading around $\xi_{992}=2.036$) and eight collective modes are found in the tail. The corresponding values of $\bar{E}_j$, calculated from the theory (29) and from the spectra, are given in Table III. Fluctuation measures, $P(S)$ and $\Sigma^2(r)$, for the bulk of the spectra are in agreement with the GOE and shown in respectively Fig. 21(a) and 21(b).

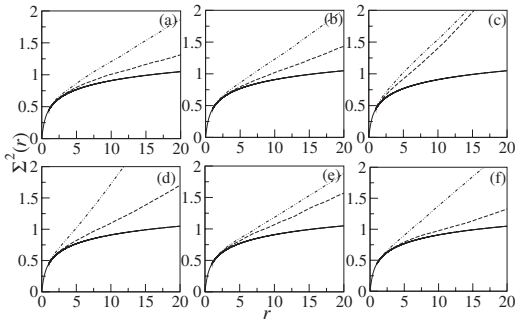

FIG. 17. Number variance for the θ and p variable of the Standard map where $K=2$. Figures (a), (b), and (c) are for the θ variable respectively for the ranges (i), (ii), and (iii) given in text. Figures (d), (e), and (f) are for the p variable respectively for the ranges (i), (ii), and (iii) given in text. Solid lines represent GOE, dashed lines represent $N=1000$ case where as dashed line with dots represent $N=200$ case.

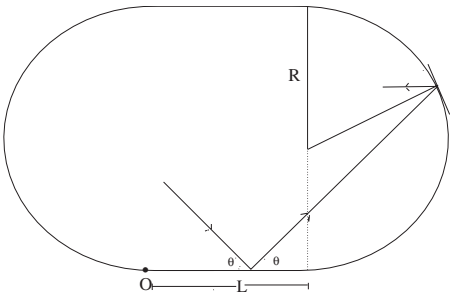

FIG. 18. Stadium billiard.

For the p variable, $C(\zeta)=\exp(-a\zeta^b)$ for $\zeta>5$, where $a=0.229\,86$, $b=0.755\,49$. Though hardly visible in Fig. 22(a), $C(\zeta)=1-a_0\zeta$ when $\zeta\leq 2$, $C(\zeta)=1-2a_0-a_1(\zeta-2)$ when $2\leq\zeta\leq 4$ and $C(5)=1-2a_0-2a_1-a_2$. Here, the coefficients are given by $a_0=0.178\,239\,5$, $a_1=0.0501056$, and $a_2=0.081\,042$. Spectrum of the correlation matrix is obtained the range $0.042\,43\leq\xi_j\leq 16.5049$ as shown in Fig. 22(b). In Fig. 22(c), we show $\sigma^2\xi_j$ where $0.09\leq\xi_j\leq 0.66$. Level density is obtained in the range $0.0113\leq x\leq 5.61$ and shown in Fig. 22(d). Several collective modes have been obtained in the tail and some of them are shown in the inset of Fig. 22(d). The two peaks of the density in the main graph of Fig. 22(d) belong to the nearly continuous spectrum of the ξ_js, see Fig. 22(c) for comparison.

As shown in Fig. 23(a), the spacing distribution is in agreement with the GOE. We have shown the two-point comparison function in Fig. 23(b). The number variance, as suggested by the comparison plot, is found to be consistent

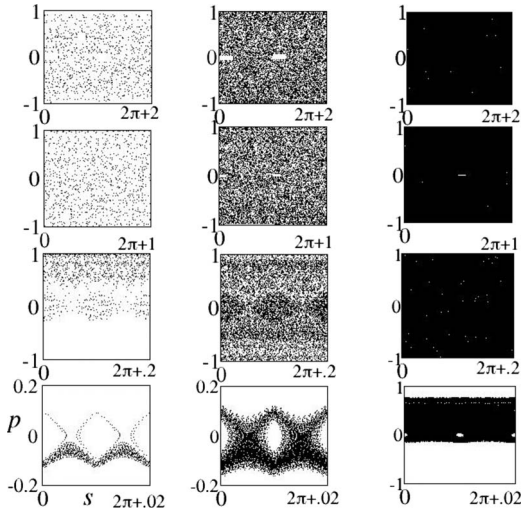

FIG. 19. Phase plots for Stadium billiard, for $L=1$, 0.5, and 0.10.01 (respectively, for each row of boxes from top to bottom) and for 10^3, 10^4, and 10^5 number of iterations (respectively for each column for boxes from left to right).

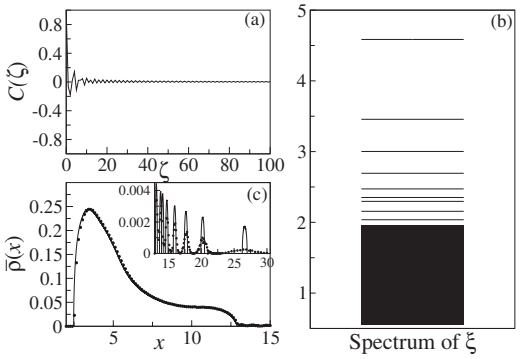

FIG. 20. $C(\zeta)$, spectrum of ξ and $\bar{\rho}(x)$, respectively, in figure (a), (b), and (c) for the s variable of the Stadium billiard for $L=1$. Eight collective modes are obtained in the tail of the level density as shown in the inset. Solid lines in figure (c) represent RMT and dots represent simulations.

with the GOE only for the ranges $0.0114 \leq x \leq 0.02$ and $0.08 \leq x \leq 0.18$. We have analyzed the number variance for four ranges, viz. (i) $0.0114 \leq x \leq 0.02$, (ii) $0.02 \leq x \leq 0.08$, (iii) $0.08 \leq x \leq 0.18$, and (iv) $0.18 \leq x \leq 1.0$. For these ranges the number variances are shown respectively in Figs. 24(a)–24(d). From each spectrum there are around 232 levels in (i), 180 levels in (ii), 326 levels in (iii), and 181 levels in (iv). The agreement with the GOE is excellent as shown in Figs. 24(a) and 24(c) but there are significant departures in Figs. 24(b) and 24(d).

The same analysis has been repeated for $L=0.5$. We have considered 500 independent time series, as mentioned before. For the s variable the ξ spectrum is found in the range $0.494\,37 \leq \xi_j \leq 1.9001$ and the level density is found in the range $1.730 \leq x \leq 9.289$. As in the previous case, the density as well as the fluctuations are found to be in good agreement with the theory. These are shown in Figs. 25 and 26. However, no collective mode is obtained in this case.

For the p variable, $a=0.064\,095$, $b=0.859\,65$ for $\zeta \geq 9$, $0.0132 \leq \xi_j \leq 51.997$ and $0.003\,43 \leq x \leq 17.4347$. $C(\zeta)$, spectrum of ξ and $\bar{\rho}(x)$ are shown in Fig. 27. Spacing distribution and the two-point comparison plot are shown respectively in

TABLE III. Table for the $\bar{E}_j$ corresponding to the collective modes shown in the inset of Fig. 20(c), for the s variable of the stadium billiard with $L=1$.

j (Index)	ξ_j	$\bar{E}_j$ (Theory)	$\bar{E}_j$ (Simulation)
992	11.6447	12.8194	12.7991
993	12.3292	13.1607	13.0868
994	13.1327	13.8001	13.5450
995	13.4434	14.1224	14.0628
996	14.1385	14.7576	14.8321
997	15.3999	15.9476	15.9627
998	17.1652	17.6579	17.6571
999	19.7657	20.2138	20.2294
1000	26.2195	26.6104	26.7367

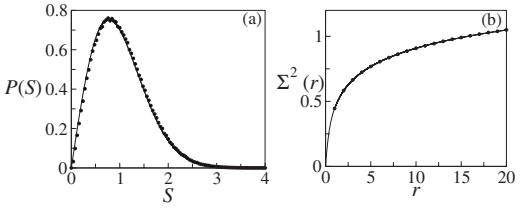

FIG. 21. $P(S)$ and $\Sigma^2(r)$ respectively in figure (a) and (b) for the s variable of the Stadium billiard for $L=1$. Solid lines represent GOE and dots represent simulations.

Figs. 28(a) and 28(b). As in the previous case, here also we have investigated the number variance in four ranges, viz. (i) $0.0003 \leq x \leq 0.007$, (ii) $0.007 \leq x \leq 0.05$, (iii) $0.05 \leq x \leq 0.075$, and (iv) $0.075 \leq x \leq 1.0$. From each spectrum, range (i) contains around 323 levels, (ii) contains around 209 levels, (iii) contains around 185 levels and (iv) contains around 229 levels. $\Sigma^2(r)$ is again found to in agreement with the GOE for (i) and (iii) and it deviates from the GOE for (ii) and (iv). These are shown in Fig. 29 for the respective the ranges.

XI. DECORRELATED ENSEMBLES

We have also analyzed the spectra of $\xi^{-1/2} H \xi^{-1/2}$ matrices. By this transformation we have removed the correlation effects, thus one expects agreement of the level density as well as the fluctuation measures with the uncorrelated case. In Fig. 30, we show the analysis of the *decorrelated* spectra for $c=0.9$ of the Gaussian time series. We remark that the collective modes have disappeared after decorrelation. This happens because the collective modes are remnants of the corresponding modes in the correlation matrix ξ. We have done this analysis for several cases we have considered in this paper, and found agreement with the uncorrelated ensemble.

XII. DISCUSSIONS AND CONCLUSION

We have presented a study of the correlated Wishart ensembles in the context of time series analysis. Using the

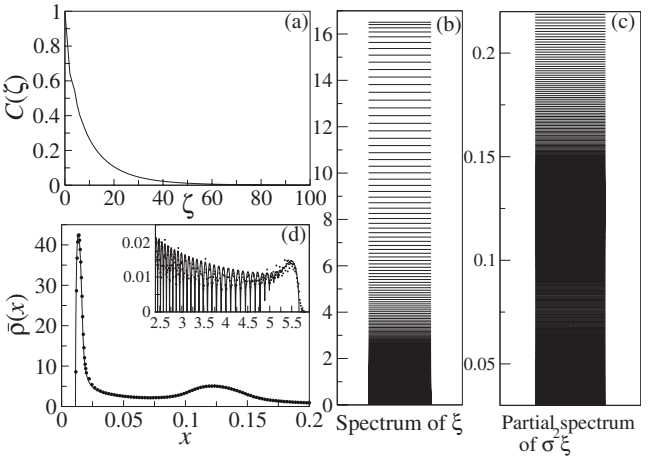

FIG. 22. $C(\zeta)$, full spectrum of ξ, enlarged lower portion of the spectrum of $\sigma^2\xi$ and $\bar{\rho}(x)$ respectively in figure (a), (b), (c), and (d) for the p variable of the Stadium billiard for $L=1$.

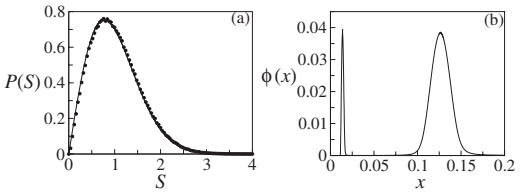

FIG. 23. $P(S)$ and $\Phi(x)$, respectively, in figure (a) and (b) for the p variable of the Stadium billiard for $L=1$. Solid line in figure (a) represents RMT and dots represent simulations.

binary correlation method for large random matrices we have derived exact result for the level density Eq. (16) and approximate result for the two-point correlation function (41). The two-point function is of direct use in the random matrices of the time series analysis but can also be useful in other contexts [6,7,30,36]. We have also derived mean positions of the isolated levels (collective modes) and their variances Eqs. (29) and (30). These are useful in studying the effects of correlations on the collective behavior of the time series.

To test our analytic results we have first considered the stochastic time series with exponentially decaying correlations. In this case we find that when the correlation c is small or moderate, the level density differs from the Marčenko-Pastur law but no collective mode is observed. In spite of correlations, spectral fluctuations are found to be universal everywhere. On the other hand when the correlations become stronger, the spectra exhibit mixed fluctuation properties; majority of eigenlevels have universal fluctuations whereas for small portion of spectra long range fluctuations are not universal. These spectral regions can be characterized by one of the three cases, viz. (a) eigenlevels have universal fluctuations, (b) eigenlevels show departure from universality for long range correlations, and (c) a few eigenlevels are isolated and the spectrum has collective modes. We have also shown that our results [Eqs. (29) and (42)] have been useful in characterizing these three spectral regions. We find that the spacing distribution is consistent with the Wigner surmise in cases (a) and (b), confirming thereby the universality of the short range fluctuations. The deviations in case (b) are for larger r values in $\Sigma^2(r)$, indicating the breakdown of universality for long range statistics.

From a similar analysis for the Arnold map, where autocorrelation dies almost immediately, we find the Marčenko-

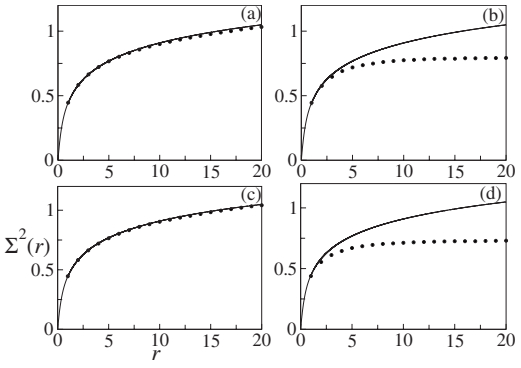

FIG. 24. $\Sigma^2(r)$, respectively, for the ranges (i), (ii), (iii), and (iv) of the p variable of the Stadium billiard for $L=1$. Solid lines represent RMT and dots represent simulations.

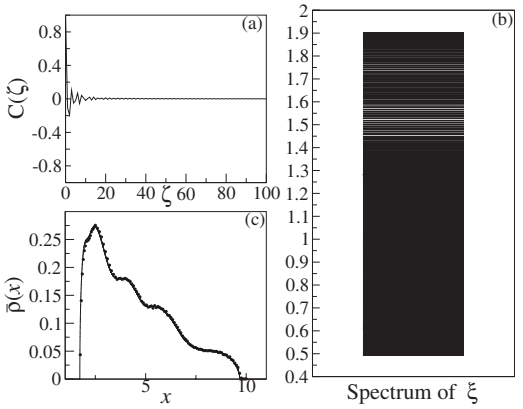

FIG. 25. $C(\zeta)$, spectrum of ξ and $\bar{\rho}(x)$, respectively, in figure (a), (b), and (c) for the s variable of the Stadium billiard for $L=0.5$. Solid line in figure (c) represents RMT and dots represent simulations.

Pastur law for the level density and universal spectral fluctuations everywhere for the time series of both the variables. This analysis verifies the universality which is expected from the time series of uncorrelated variables.

As we know that the standard map is largely chaotic for $K>5$ and there are integrable regions in the phase space for $K\lesssim 5$. For $K=5$, our analysis yields collective modes for the time series of both the variables. In contrast, we find no collective mode for $K=10$ where there is no apparent stable island. In fact for very large values of K ($K\gtrsim 100$ where the integrable regions are almost absent) we find the Marčenko-Pastur law for the level density and universal spectral fluctuations everywhere. For $K\lesssim 10$ the correlation functions do not look very different from each other but their differences are visible in spectral analysis, e.g., emergence of the collective modes. They are explicit in the level density as they give different shapes of the level density. It has been shown recently [37] that the phase space has small stable island structures for $K=9.26$. What one expects from this analysis is the presence of collective modes for this values of K. Indeed this analysis gives collective modes for $K=9.26$. All these naturally go in favor of the remark that the collective modes indicate presence of islands and the analysis can be used for multidimensional chaotic maps in probing the existence of integrable regions. It would be worth investigating this correspondence more precisely and accurately.

In the analysis of stadium billiard map for $L=1.0$, we find that the spectra for the p variable have all the three cases, viz. (a), (b), and (c) while spectra of the s variable does not

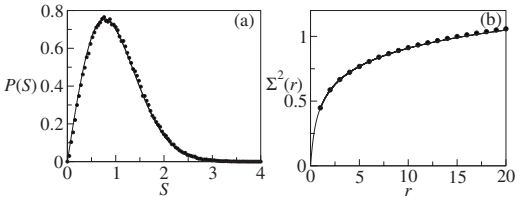

FIG. 26. $P(S)$ and $\Sigma^2(r)$, respectively, in figure (a) and (b) for the s variable of the Stadium billiard for $L=0.5$. Solid lines represent RMT and dots represent simulations.

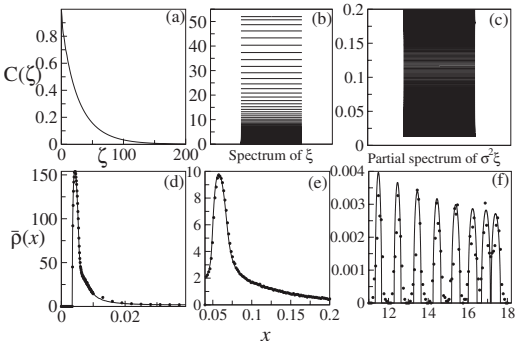

FIG. 27. $C(\zeta)$, full spectrum of ξ, lower portion of the spectrum of $\sigma^2\xi$ and $\bar{\rho}(x)$ respectively in figure (a), (b), (c), and (d) for the p variable of the Stadium billiard for $L=0.5$. The level density has a long tail. In figures (d) and (e) we show the two peaks of the density observed in the range $0.0114 \leq x \leq 0.2$. Several collective modes are obtained in the tail as some of them are shown in figure (f), near the upper cutoff of the density. In figures (d, e, f) solid lines represent RMT and dots represent simulations.

exhibit the case (b). The same analysis for $L=0.5$, where $C(\zeta)$ dies very rapidly for the s variable, yields only the case (a) in the spectral statistics. In contrast, for the p variable, number of collective modes becomes even larger, since $C(\zeta)$ grows for the smaller values of L. These effects are most likely caused by the marginally stable orbits rendered due to the small L values. It would be interesting to analyze these behaviors for large L values where the autocorrelation function is oscillatory for both the variables. In this case effects of the bouncing ball orbits should be visible in the analysis [38].

Finally, we remark that the location of the spectral regions corresponding to the cases (a) and (b) depends on the very nature of the correlations. For example, for $C(\zeta)=c^{\zeta}$ where c is large, (a) is obtained for the smaller eigenlevels and (b) is found for the intermediate eigenlevels in the spectra. However there are situations, e.g., in the analysis for the p variable of stadium billiard, (a) and (b) are found twice at two different locations in spectra for both values of L. We also remark that this happens even though $C(\zeta)$ is slightly different from the stretched exponential where one gets qualitatively similar results as those for the exponentially decaying autocorrelations. For the case (c) which has been seen mostly in the tails may also be found in the middle of the spectra with multiply banded level densities. It would be worth investigating the level density and fluctuations at the hard edge for the correlated Wishart ensembles, analogus to the earlier studies of the Wishart ensembles or chiral-random matrix ensembles [39–42].

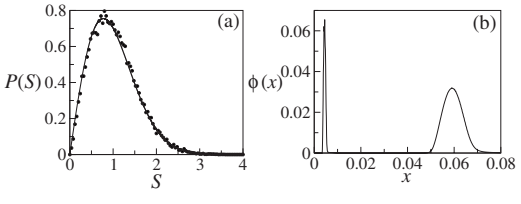

FIG. 28. $P(S)$ and $\Phi(x)$, respectively, in figure (a) and (b) for the p variable of the Stadium billiard for $L=0.5$. In figure (a), solid line represents RMT and dots represent simulations.

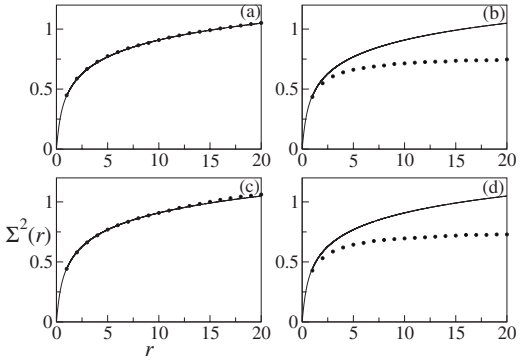

FIG. 29. $\Sigma^2(r)$, respectively, for the ranges (i), (ii), (iii), and (iv) of the p variable of the Stadium billiard for $L=0.5$. Solid lines represent RMT and dots represent simulations.

ACKNOWLEDGMENT

One of us (Vinayak) acknowledges UGC, India, for financial support.

APPENDIX A: PROOF OF EQUATION (29) and (30)

To derive Eq. (30), we write first the resolvent as

$$\bar{G}(z) = \Phi(z) + \frac{1}{N}\Theta(z), \tag{A1}$$

where

$$\Phi(z) = \left\langle Q_k \frac{1}{z - \sigma^2[\kappa - 1 + z\bar{G}(z)]\xi/\kappa} \right\rangle \tag{A2}$$

and

$$\Theta(z) = \frac{1}{z - \bar{E}_k}. \tag{A3}$$

The inverse transform of Eq. (A3) yields the delta function in the result Eq. (29). Next, we write $\bar{G}_{\xi}=\Phi_{\xi}(z)+\frac{1}{N}\Theta_{\xi}(z)$, where

$$\Phi_{\xi}(z) = \left\langle Q_k \xi \frac{1}{z - \sigma^2[\kappa - 1 + z\bar{G}(z)]\xi/\kappa} \right\rangle \tag{A4}$$

and

$$\Theta_{\xi}(z) = \frac{\xi_k}{z - \bar{E}_k}. \tag{A5}$$

For the isolated level, the two-point resolvent is given by

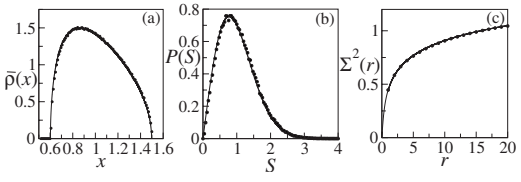

FIG. 30. $\bar{\rho}(x)$, P(s), and $\Sigma^2(r)$ after the decorrelation of time series. Solid lines represent RMT and dots represent simulations.

$$N^2 S^G_{\rm iso}(z_1,z_2) = \overline{[(z_1-E_k)(z_2-E_k)]^{-1}} - \overline{(z_1-E_k)^{-1}}\;\overline{(z_2-E_k)^{-1}}$$
$$= (\Theta(z_1)\Theta(z_2))^2\overline{(\delta E_k)^2}. \tag{A6}$$

Here the second equality is derived by using the expansion $E_k=\bar{E}_k+\delta E_k$ in the first equality. Now using Eq. (A1) in Eqs. (36) and (37) we get

$$S^G_{\rm iso} \equiv S^G - S^G_0 = -\frac{2\sigma^2}{\kappa\beta N^3}\frac{\partial^2}{\partial z_1\,\partial z_2}\left\{\left[\frac{z_1\Theta_\xi(z_1)-z_2\Theta_\xi(z_2)}{z_1-z_2}\right]\right.$$
$$\left.\times\left[1-\frac{z_1\Phi_\xi(z_1)-z_2\Phi_\xi(z_2)}{z_1-z_2}\right]^{-1}\right\}. \tag{A7}$$

We have

$$\frac{z_1\Theta(z_1)-z_2\Theta(z_2)}{z_1-z_2} = -\xi_k\bar{E}_k\Theta(z_1)\Theta(z_2), \tag{A8}$$

$d\Theta(z)/dz=-[\Theta(z)]^2$. Next using Eqs. (A6) and (A7) and ignoring contribution from partial derivatives of the second term of Eq. (A7) in the neighborhood of $z=\bar{E}_k$, we get

$$\overline{(\delta E_k)^2} = \frac{2\sigma^2\xi_k\bar{E}_k}{\kappa\beta N}\left[1-\frac{d}{dz}z\Phi_\xi(z)\big|_{z=\bar{E}_k}\right]^{-1}. \tag{A9}$$

For derivative in Eq. (A9), we find

$$\frac{d}{dz}z\Phi_\xi(z) = \frac{\langle Q_k\xi\varphi\rangle - z\langle Q_k\xi\varphi^2\rangle}{1-z\sigma^2\langle Q_k\xi\varphi^2\rangle/\kappa}, \tag{A10}$$

where

$$\varphi = (z-\sigma^2(\kappa-1+z\Phi)\xi/\kappa)^{-1}. \tag{A11}$$

Finally, using Eq. (A10) in Eq. (A9) along with Eq. (25) for the k-th isolated nondegenrate level, we get Eq. (30).

APPENDIX B: DETAILS OF EQUATIONS (36) and (37)

Using Eq. (35) and $\overline{\delta m_0\delta m_q^{L_2}}=\overline{\delta m_p\delta m_0^{L_2}}=0$ for $p,q\geq 0$ in Eq. (32) we get

$$\overline{\delta G_{L_1}\delta G_{L_2}} = \frac{\sigma^2}{z_1}\overline{\delta G_{L_1\xi}\delta G_{L_2}} + \frac{\sigma^2}{\kappa}[\overline{\delta G_{L_1\xi}\delta G_{L_2}}(\bar{G}(z_1)-z_1^{-1}) + \overline{\delta G(z_1)\delta G_{L_2}}\bar{G}_{L_1\xi}]$$
$$+\frac{\sigma^2}{\kappa N^2}\left\{\overline{\langle L_1\xi(z_2-H)^{-1}L_2(z_2-H)^{-1}[(z_1-H)^{-1}-z_1^{-1}]\rangle} + \frac{(2-\beta)}{\beta}\overline{\langle L_1\xi(z_2-H)^{-1}\tilde{L}_2(z_2-H)^{-1}[(z_1-H)^{-1}-z_1^{-1}]\rangle}\right\}. \tag{B1}$$

We have used here $S^G_{L_1,L_2}\equiv\overline{\delta G_{L_1}(z_1)\delta G_{L_2}(z_2)}$ and an abbreviation $\overline{\delta G_{L_1}\delta G_{L_2}}$ for $\overline{\delta G_{L_1}(z_1)\delta G_{L_2}(z_2)}$ and for other related quantities. Next we simplify this equation with the help of the relation

$$\overline{\delta G_{L_1}\delta G_{L_2}} \equiv \mathcal{F}(L_1\Gamma_1^{-1},L_2), \tag{B2}$$

for $\overline{\delta G_{L_1\Gamma_1}\delta G_{L_2}}\equiv\mathcal{F}(L_1,L_2)$ where inverse of the operator Γ_1 exists. A twice use of this relation leads to

$$\overline{\delta G_{\Gamma_1}\delta G_{L_2}} = \frac{z_1\sigma^2}{\kappa N^2}\left\{\overline{\langle L_1Y_1\xi(z_2-H)^{-1}L_2(z_2-H)^{-1}[(z_1-H)^{-1}-z_1^{-1}]\rangle} + \frac{(2-\beta)}{\beta}\overline{\langle L_1Y_1\xi(z_2-H)^{-1}\tilde{L}_2(z_2-H)^{-1}[(z_1-H)^{-1}-z_1^{-1}]\rangle}\right\}, \tag{B3}$$

where

$$Y(z) \equiv \overline{\frac{1}{z-H}} = \frac{1}{z-\dfrac{\sigma^2}{\kappa}[\kappa-1+z\bar{G}(z)]\xi} \tag{B4}$$

and $\Gamma=L-z\sigma^2\langle LY\xi Y\rangle/\kappa$. It follows from the definition that $\langle Y(z)\rangle=\bar{G}(z)$. We prefer to write $\overline{\delta G_{\Gamma_1}\delta G_{L_2}}$ as $\overline{\delta G_{L_1}\delta G_{L_2}}$ and find

$$\overline{\delta G_{L_1}\delta G_{L_2}} = \frac{z_1\sigma^2}{\kappa N^2}\left\{\overline{\langle \mathcal{L}_1Y_1\xi(z_2-H)^{-1}L_2(z_2-H)^{-1}[(z_1-H)^{-1}-z_1^{-1}]\rangle} + \frac{(2-\beta)}{\beta}\overline{\langle \mathcal{L}_1Y_1\xi(z_2-H)^{-1}\tilde{L}_2(z_2-H)^{-1}[(z_1-H)^{-1}-z_1^{-1}]\rangle}\right\}, \tag{B5}$$

where $\mathcal{L}$ is given by

$$\mathcal{L} = L + \frac{z\sigma^2}{\kappa}\langle LY\xi Y\rangle\left(1-\frac{z\sigma^2}{\kappa}\langle\xi YY\rangle\right)^{-1}. \tag{B6}$$

Now we use $L_1=L_2=\mathbf{1}$ and obtain

$$\overline{\delta G(z_1)\delta G(z_2)} = \frac{2\sigma^2}{\kappa\beta N^2}\left(1 - \frac{z_1\sigma^2}{\kappa}\langle \xi Y_1 Y_1\rangle\right)^{-1} \times \frac{\partial}{\partial z_2}\left[\frac{z_1\langle \xi Y_1 Y_1\rangle - z_2\langle \xi Y_2 Y_1\rangle}{z_1 - z_2}\right]. \tag{B7}$$

Finally use of the identity

$$\frac{\partial}{\partial z_1}\ln\left[1 - \frac{\sigma^2}{\kappa}\frac{z_1\langle \xi Y_1\rangle - z_2\langle \xi Y_2\rangle}{(z_1 - z_2)}\right] = \frac{\sigma^2}{\kappa}\left(1 - \frac{z_1\sigma^2}{\kappa}\langle \xi Y_1 Y_1\rangle\right)^{-1}\left[\frac{z_1\langle \xi Y_1 Y_1\rangle - z_2\langle \xi Y_2 Y_1\rangle}{z_1 - z_2}\right] \tag{B8}$$

in Eq. (B7) gives Eqs. (36) and (37).

APPENDIX C: STADIUM BILLIARD MAP

The map is described in four parts depending on the initial position s_0. These four parts divided into subparts for different values of the initial conjugate momentum p_0. One of the joining of arcs with the straight line is taken as the fixed point or the reference point "O" as shown in Fig. 18.

(i) $0 \le s_0 < L$

Let

$$P_1 = \frac{L - s_0}{\sqrt{4R^2 + (L - s_0)^2}}, \tag{C1}$$

$$P_2 = -\frac{s_0}{\sqrt{4R^2 + s_0^2}}. \tag{C2}$$

Then for $P_1 \le p_0 < 1$,

$$p_1 = p_0 - \frac{L - s_0}{R}\sqrt{(1 - p_0^2)}, \tag{C3}$$

$$s_1 = L + R(\cos^{-1} p_0 + \cos^{-1} p_1). \tag{C4}$$

For $P_2 \le p_0 < P_1$,

$$p_1 = -p_0, \tag{C5}$$

$$s_1 = 2L + \pi R - s_0 - 2R\frac{p_0}{\sqrt{1 - p_0^2}}. \tag{C6}$$

For $-1 \le p_0 < P_2$,

$$p_1 = p_0 - \frac{s_0}{R}\sqrt{(1 - p_0^2)}, \tag{C7}$$

$$s_1 = 2L + R(\cos^{-1} p_0 + \cos^{-1} p_1). \tag{C8}$$

(ii) $L \le s_0 < (L + \pi R)$

Let

$$P_3 = \sin\left(\frac{s_0 - L}{2R}\right), \tag{C9}$$

$$P_4 = -\cos\left(\frac{s_0 - L}{R}\right)\cos(\tan^{-1}\omega^+) + \sin\left(\frac{s_0 - L}{R}\right)\sin(\tan^{-1}\omega^+), \tag{C10}$$

$$P_5 = -\cos\left(\frac{s_0 - L}{R}\right)\cos(\tan^{-1}\omega^-) - \sin\left(\frac{s_0 - L}{R}\right)\sin(\tan^{-1}\omega^-), \tag{C11}$$

$$P_6 = -\cos\left(\frac{s_0 - L}{2R}\right), \tag{C12}$$

where

$$\omega^{\pm} = \frac{R\left[1 \pm \cos\left(\frac{s_0 - L}{R}\right)\right]}{L + R\sin\left(\frac{s_0 - L}{R}\right)}. \tag{C13}$$

Then for $P_3 \le p_0 < 1$,

$$p_1 = p_0, \tag{C14}$$

$$s_1 = s_0 + 2R\cos^{-1} p_0. \tag{C15}$$

For $P_4 \le p_0 < P_3$,

$$p_1 = -p_0\cos\left(\frac{s_0 - L}{R}\right) + \sqrt{(1 - p_0^2)}\sin\left(\frac{s_0 - L}{R}\right), \tag{C16}$$

$$s_1 = L + \pi R - R\sin\left(\frac{s_0 - L}{R}\right) + \frac{Rp_1}{\sqrt{1 - p_1^2}}\left[1 + \cos\left(\frac{s_0 - L}{R}\right)\right]. \tag{C17}$$

For $P_5 \le p_0 < P_4$,

$$p_1 = p_0 + \frac{L}{R}(\sqrt{1 - p_0^2})\cos\left(\frac{s_0 - L}{R}\right) + \frac{L}{R}p_0\sin\left(\frac{s_0 - L}{R}\right), \tag{C18}$$

$$s_1 = s_0 + L + R(\cos^{-1} p_0 + \cos^{-1} p_1). \tag{C19}$$

For $P_6 \le p_0 < P_5$,

$$p_1 = p_0\cos\left(\frac{s_0 - L}{R}\right) - \sqrt{(1 - p_0^2)}\sin\left(\frac{s_0 - L}{R}\right), \tag{C20}$$

$$s_1 = L + R\sin\left(\frac{s_0 - L}{R}\right) + \frac{Rp_1}{\sqrt{1 - p_1^2}}\left[1 - \cos\left(\frac{s_0 - L}{R}\right)\right]. \tag{C21}$$

For $-1 < p_0 \le P_6$,

$$p_1 = p_0 \tag{C22}$$

$$s_1 = s_0 + 2R\cos^{-1} p_0 - 2\pi R \tag{C23}$$

(iii) $(L+\pi R) \leq s_0 < (2L+\pi R)$.

Equation for this part can be obtained from part (i), replacing s_0 by $s_0 - L - \pi R$ and s_1 by $s_1 - L - \pi R$.

(iv) $(2L+\pi R) \leq s_0 < (2L+2\pi R)$.

Equation for this part can be obtained from part (ii), replacing s_0 by $s_0 - L - \pi R$ and s_1 by $s_1 - L - \pi R$.

[1] M. L. Mehta, *Random Matrices* (Academic Press, New York, 2004).
[2] J. Wishart, Biometrika **A20**, 32 (1928).
[3] S. S. Wilks, *Mathematical Statistics* (Wiley, New York, 1962).
[4] L. Laloux, P. Cizeau, J. P. Bouchaud, and M. Potters, Phys. Rev. Lett. **83**, 1467 (1999).
[5] V. Plerou, P. Gopikrishnan, B. Rosenow, L. A. Nunes Amaral, and H. E. Stanley, Phys. Rev. Lett. **83**, 1471 (1999).
[6] E. Telatar, Eur.Trans.Telecomm. **10** (6), 585 (1999).
[7] S. H. Simon and A. L. Moustakas, Phys. Rev. E **69**, 065101(R) (2004).
[8] Y. Demasure and R. A. Janik, Phys. Lett. B **553**, 105 (2003).
[9] A. Lakshminarayan, S. Tomsovic, O. Bohigas, and S. N. Majumdar, Phys. Rev. Lett. **100**, 044103 (2008).
[10] P. J. Forrester and T. D. Huges, J. Math. Phys. **35**, 6736 (1994).
[11] F. Lou, J. Zhong, Y. Yang, and J. Zhou, Phys. Rev. E **73**, 031924 (2006).
[12] S. Abe and N. Suzuki, e-print arXiv:0909.3830.
[13] A. Pandey and S. Ghosh, Phys. Rev. Lett. **87**, 024102 (2001); S. Ghosh and A. Pandey, Phys. Rev. E **65**, 046221 (2002).
[14] T. A. Brody, J. Flores, J. B. French, P. A. Mello, A. Pandey, and S. S. M. Wong, Rev. Mod. Phys. **53**, 385 (1981).
[15] F. Haake, *Quantum Signatures of Chaos* (Springer, Berlin, 1991).
[16] C. W. J. Beenakker, Rev. Mod. Phys. **69**, 731 (1997).
[17] M. S. Santhanam and P. K. Patra, Phys. Rev. E **64**, 016102 (2001).
[18] P. Šeba, Phys. Rev. Lett. **91**, 198104 (2003).
[19] M. S. Santhanam and H. Kantz, Phys. Rev. E **69**, 056102 (2004).
[20] V. Kulkarni and N. Deo, Eur. Phys. J. B **60**, 101 (2007).
[21] A. M. Sengupta and P. P. Mitra, Phys. Rev. E **60**, 3389 (1999).
[22] Z. Burda, J. Jurkiewicz, and B. Waclaw, Phys. Rev. E **71**, 026111 (2005).
[23] H. Gao and P. J. Smith, J. Multivariate Anal. **73**, 155 (2000).
[24] Y. Malevergne and D. Sornette, Physica A **331**, 660 (2004).
[25] J. W. Silverstein, J. Multivariate Anal. **55**, 331 (1995).
[26] A. Pandey, Ann. Phys. (N.Y.) **134**, 110 (1981).
[27] A. Pandey and J. B. French, J. Phys. A **12**, L83 (1979).
[28] A. J. Lichtenberg and M. A. Lieberman, *Regular and Chaotic Dynamics* (Springer, Verlag, 1992).
[29] L. A. Bunimovich, Commun. Math. Phys. **65**, 295 (1979).
[30] R. R. Muller, IEEE Trans. Inf. Theory **48**, 2495 (2002).
[31] S. K. Sarkar, G. S. Matharoo, and A. Pandey, Phys. Rev. Lett. **92**, 215503 (2004).
[32] Vinayak, Ph.D. thesis, Jawaharlal Nehru University (unpublished).
[33] V. A. Marčenko and L. A. Pastur, Mat. Sb. **72**, 507 (1967);F. J. Dyson, Rev. Mex. Fis. **20**, 231 (1971).
[34] I. M. Johnstone, Ann. Stat. **29**, 295 (2001).
[35] J. Baik, G. Ben Arous, and S. Péché, Ann. Probab. **33**, 1643 (2005).
[36] J. Jurkiewicz, G. Łukaszewski, and M. A. Nowak, Acta Phys. Pol. B **39**, 799 (2008).
[37] S. Tomsovic and A. Lakshminarayan, Phys. Rev. E **76**, 036207 (2007).
[38] H. J. Stöckmann, *Quantum Chaos: An Introduction* (Cambridge University Press, Cambridge, 1999).
[39] J. Z. Ma, T. Guhr, and T. Wetting, Eur. Phys. J. A **2**, 87 (1998).
[40] J. Verbaarschot, Nucl. Phys. B **426**, 559 (1994).
[41] T. Nagao and P. J. Forrester, Nucl. Phys. B **435**, 401 (1995).
[42] S. Nishigaki, Phys. Lett. B **387**, 139 (1996).